Main Manuscript for

Harnessing AlphaFold to reveal state secrets: Prediction of hERG closed and inactivated states

Khoa Ngo*[1,2,5], Vladimir Yarov-Yarovoy[2,3], Colleen E. Clancy*[2,4,5] and Igor Vorobyov*[2,4]

[1]Biophysics Graduate Group, University of California, Davis, CA
[2]Department of Physiology and Membrane Biology, University of California, Davis, CA
[3]Department of Anesthesiology and Pain Medicine, University of California, Davis, CA
[4]Department of Pharmacology, University of California, Davis, CA
[5]Center for Precision Medicine and Data Science, University of California, Davis, CA
*Corresponding authors

Email: khoango@ucdavis.edu, ceclancy@ucdavis.edu, ivorobyov@ucdavis.edu

Short title: AlphaFold application to reveal hERG channel states

Author Contributions: K.N. conducted simulations, acquired data, analyzed data, and wrote the manuscript. V.Y.-Y., C.E.C., and I.V. designed the research study, analyzed data, and wrote the manuscript.

Competing Interest Statement: The authors declare no competing interests.

Classification: Biological Sciences, Biophysics and Computational Biology

Keywords: Voltage-gated potassium channel, hERG, AlphaFold, molecular docking, molecular dynamics simulation

This file includes:

Main Text
Figures 1 to 9

Abstract

To design safe, selective, and effective new therapies, there must be a deep understanding of the structure and function of the drug target. One of the most difficult problems to solve has been resolution of discrete conformational states of transmembrane ion channel proteins. An example is $K_V11.1$ (hERG), comprising the primary cardiac repolarizing current, I_{Kr}. hERG is a notorious drug anti-target against which all promising drugs are screened to determine potential for arrhythmia. Drug interactions with the hERG inactivated state are linked to elevated arrhythmia risk, and drugs may become trapped during channel closure. However, the structural details of multiple conformational states have remained elusive. Here, we guided AlphaFold2 to predict plausible hERG inactivated and closed conformations, obtaining results consistent with myriad available experimental data. Drug docking simulations demonstrated hERG state-specific drug interactions aligning well with experimental results, revealing that most drugs bind more effectively in the inactivated state and are trapped in the closed state. Molecular dynamics simulations demonstrated ion conduction that aligned with earlier studies. Finally, we identified key molecular determinants of state transitions by analyzing interaction networks across closed, open, and inactivated states in agreement with earlier mutagenesis studies. Here, we demonstrate a readily generalizable application of AlphaFold2 as a novel method to predict discrete protein conformations and novel linkages from structure to function.

Significance Statement

It has been a longstanding goal to reveal the distinct conformational states of proteins to better understand their function. In pursuit of this goal, an extensive array of approaches including mutagenesis, electrophysiological, structural and computational methods have been undertaken. While published studies have yielded important insights, none of the existing approaches have proven adequate to unambiguously identify natural protein conformational states. Here, we demonstrate the successful application of deep-learning based AlphaFold2 to predict conformational states of the key cardiac hERG K^+ ion channel. The implications are broad as understanding hERG is critical for drug cardiac safety. Moreover, the approach can be readily generalized to other ion channels, offering a versatile framework for identifying protein structure and its link to function.

Introduction

The human voltage-gated potassium channel $K_V11.1$, encoded by the KCNH2 or human Ether-à-go-go-Related Gene (hERG) gene, is a key player in cardiac electrophysiology, underpinning the rapid component of the delayed rectifier K^+ current (I_{Kr}) in cardiac myocytes(1). This current plays a crucial role in the repolarization phase of the cardiac action potential, essential for the rhythmic and stable electrical propagation and consequent contraction(2). Perturbation to hERG channel function, whether stemming from genetic anomalies or pharmacological interventions, can precipitate multiple arrhythmogenic disorders(2).

The distinctive pharmacological sensitivity of hERG channels, prone to blockade by a diverse array of drugs, has placed them at the forefront of cardiac safety pharmacology and the drug discovery process. Blockade of hERG by drugs can lead to QT interval prolongation known as an acquired long QT syndrome and escalate the risk of *torsades de pointes* (TdP), a potentially fatal arrhythmia(3). This issue has prompted the withdrawal of various drugs from the market and underscored the necessity of incorporating hERG safety evaluations in the drug development pipeline(4–6).

The hERG channel is a homotetramer, with each subunit containing six membrane-spanning segments (S1-S6)(7). The segments S5 and S6 along with the intervening loops and short pore helix form the channel pore domain (PD), crucial for potassium ion passage, while segments S1-S4 form the voltage sensing domain (VSD), responding to voltage changes across the cell membrane. Notably, the hERG channel also features specialized intracellular regions: the Per-Arnt-Sim (PAS) domain at the N-terminus and the cyclic nucleotide-binding domain (CNBD) at the C-terminus. The structural intricacies of the hERG channel, particularly its pore and voltage-sensing domains, render it sensitive to a variety of drugs, highlighting the imperative for intricate structural understanding of drug channel interactions to foster safer drug designs. This susceptibility is not uniform but varies depending on the channel conformational state, a phenomenon known as state-dependent drug block. Drugs may preferentially bind to and block the channel in specific states (open, closed, or inactivated), which can differentially affect cardiac repolarization and rhythm(8, 9).

Capturing the dynamic spectrum of hERG channel states poses a formidable challenge. While cryo-electron microscopy (cryo-EM) has offered invaluable insights into the open state of the channel(7, 10), a comprehensive view of the closed and inactivated states has remained elusive. Thus, even as we embark on a scientific era of explosive growth fueled by the convergence of protein structure insights, computational capabilities, and AI based modeling and synthetic data, the next frontier is marked by the need to reveal all relevant conformational states of proteins. The existing knowledge gaps constrain both predictive capabilities regarding drug – protein interactions and the creation of therapies through drug discovery to find specific and selective drugs, or in the case of hERG, to minimize adverse interactions. For example, a recent study by Yang *et al.* introduced a multiscale model framework to forecast drug-induced cardiotoxicity at cellular and tissue levels, utilizing atomistic simulations of drug interactions with hERG(11). However, the absence of hERG structural models in the inactivated and closed states limited the predictive potential of atomistic scale simulations of state-specific drug binding.

The emergence of AlphaFold2 (also known as AlphaFold 2), a protein structure prediction tool driven by machine learning, has brought a paradigm shift in structural biology(12). The proficiency of AlphaFold2 in accurately predicting protein structures presents a significant opportunity to model numerous proteins whose experimental structures remain unsolved. Nonetheless, the conventional use of AlphaFold2 tends to produce a single-state structure for the protein, which in the case of hERG corresponds to the open state. In this study, we presented a novel approach to guide AlphaFold2 to predict models of the hERG channel in the closed and inactivated states, thereby unveiling the elusive structural underpinnings of state-specific drug interactions and gating mechanisms of the channel.

We sought insights into the state-specific interactions of drugs with hERG channel, which are vital for revealing the mechanisms behind drug-induced cardiotoxicity and for designing safer pharmaceuticals. Our methodology blended advanced computational techniques to yield an exhaustive understanding of the dynamics of the hERG channel at atomistic resolution. We commenced with structural modeling using AlphaFold2, followed by drug docking simulations via Rosetta GALigandDock(13) to evaluate drug – ion channel interactions. All-atom molecular dynamics (MD) simulations were employed to investigate ion conduction attributes and dynamic channel behavior across conformational states. We also present an interaction network analysis that revealed key protein residues and domains involved in state transitions, offering a molecular framework for deciphering hERG channel gating mechanisms.

Results and Discussion

Generating hERG channel conformational states

The hERG channel undergoes transitions between closed, open, and inactivated conformational states. Experimental cryo-EM structures published so far(7, 10) appeared to resolve only one of those states (open and conducting) based on previous molecular simulation studies(11, 14, 15). To guide AlphaFold2 in generating diverse conformations pertinent to each conformational state, we integrated fragments from experimental structures, each characteristic of the discrete closed, open or inactivated state. We then utilized AlphaFold2 to explore a broad array of conformational states and generate the final structures. This approach ensured that the resulting conformations were diverse and relevant to each discrete conformational state. Inspired by the Meiler lab's successful use of AlphaFold2 for sampling alternative conformations of transporter and receptors(16–18), we expect that this method will be capable of yielding possible representations of the hERG channel in different states, offering an improvement over earlier computational methods that depended on homology modeling(19, 20).

To construct the closed state of the hERG channel, we used regions of the voltage-sensing domains (VSDs) from the rat EAG channel cryo-EM structure in its closed conformation (PDB 8EP1(21), residues H208 – H343) as a structural template and combined them with the selectivity filter (SF) region from an available hERG cryo-EM structure (PDB 5VA2(7), residues I607 – T634), as depicted in **Figure 1a**. Recognizing that the physiological closed state of the hERG channel might only partially resemble these structural elements, we sought to introduce a degree of flexibility in our model sampling process.

Due to the time-intensive process of creating multiple sequence alignments (MSA) for AlphaFold2, the ColabFold(22) software was made to streamline protein structure prediction by combining MMseqs2(23) sequence search toolkit with AlphaFold2, enhancing runtime efficiency while preserving high prediction accuracy. First, we provided this hybrid structure as a template for ColabFold. ColabFold utilized only a portion of the MSA in the modeling process to reduce memory usage. We adjusted the limit to 256 cluster centers and 512 additional sequences, a reduction from the standard 512 and 1024, respectively. Altering the random seed can lead to variance in cluster centers and, consequently, in structure predictions. Therefore, we set AlphaFold2 to cycle through 20 random seeds (each seed was used to produce 5 models) to foster diversity in the predicted conformational states. Additionally, we enabled the model stochastic (dropout) component during inference to sample from an ensemble of models for the more ambiguous segments of the structure prediction. Past research has indicated that these settings may permit the sampling of alternative protein conformations(16–18, 22). In total, we generated 100 models for further analysis. The N-terminal PAS domain (residues M1 – R397) was not included in the modeling due to graphics card memory limitation making the resultant model (W398 – R863) resemble hERG 1b isoform(24).

For the open hERG channel state, we utilized the existing cryo-EM structure of hERG (PDB 5VA2(7)), albeit with missing extracellular loops. We then reconstructed the extracellular loops using the Rosetta LoopRemodel mover(25) with the results shown in **Figure 1b**. This reconstructed model served as a base for molecular dynamics and drug docking simulations. However, we also wanted to test the potential for AlphaFold2 to emulate this structure. The modeling procedure was initiated with constraints akin to those used for the closed state. This time, specific regions of the putative open state hERG model (PDB 5VA2(7)) — namely the VSD (W398 – V549), the SF with adjacent pore helix (I607 – T634), a part of S6 and the cytosolic domain (S660 – R863) — were provided to ColabFold as a structural guide. Then, we generated 100 diverse models for the detailed cluster analysis.

The task of modeling hERG in an inactivated state was more complex due to the absence of direct experimental references. As illustrated in **Figure 1c**, we extracted a region of the S6 and the entire cytosolic domain (S660 – R863) from the open-state hERG channel model and employed ColabFold under similar conditions to those described above for closed and open states. Our method involved letting AlphaFold2 reconstruct the transmembrane domain from the ground up under conditions that facilitated the sampling of varied conformations(17). In the resulting models, a subset of these models exhibited SFs (residues S624 – G628) akin to the non-conductive variant observed under low extracellular K^+ conditions, as described in a preprint study by Lau *et al*.(26, 27) This non-conductive SF is primarily identified by a distinct lateral flip of the backbone carbonyl oxygens in residue V625 away from hERG central axis, creating a potential barrier that may prevent K^+ from crossing from S3 to S2 ion binding sites. We extracted this non-conductive SF and the adjacent pore helix (residues Y607 – T634) structures from our array of models and merged it with the activated VSDs (W398 – V549) and the cytosolic domain (S660 – R863) from the open-state hERG structure (PDB 5VA2(7)) to use as structural template. Employing the same parameters in ColabFold as described above, we then generated 100 more models for further analysis.

Clustering AlphaFold2-generated hERG models

Post-prediction, the resulting 100 models for each structural state were categorized into clusters based on all-atom root-mean-square deviation (RMSD) between those models, as shown in **Figure 2**, using Python scripts developed in-house. Closed-state models were clustered with a threshold of 0.75 Å across the entire channel, whereas inactivated and open states (non-empirical, AlphaFold-predicted) models focused on the SF (residues S624 – G628), with a more stringent threshold of 0.35 Å. We ranked the models in the cluster by their average per-residue confidence metric (predicted local distance difference test, or pLDDT), which assesses the likelihood that the predicted structure aligns with an experimentally determined structure(12). pLDDT above 90 are considered to be highly reliable and those between 70 and 90 as reliable with generally good protein backbone structure prediction(12). Lower scores indicate regions of lower confidence and may be unstructured. Cluster 1 is defined in this study to be the cluster with highest average pLDDT among its members.

Closed-state clusters: The analysis of closed-state clusters revealed very minor discrepancies when comparing RMSD and pLDDT values across those clusters. Comparing the top-ranked model in each cluster, the all-atom RMSD between cluster 1 (cluster with highest confidence) with cluster 2 is 0.36 Å, and with the outlier cluster is 0.95 Å (clusters with fewer than 3 members are classified as outliers). Excluding the outlier cluster, the average pLDDT scores between cluster 1 and cluster 2 are very similar. The predicted low RMSD between the models suggests a convergence of the prediction to a singular conformation, with minor differences likely arising from slight variations in the positioning of intracellular loop regions. Therefore, the top-ranked model in cluster 1 was chosen for subsequent simulations.

Inactivated-state clusters: Compared to the previous case, we observed more differences among the putative inactivated-state clusters. For this situation, we used a more precise metric for clustering by focusing exclusively on the SF (S624 – G628). Following this, we ranked the clusters according to the average pLDDT of these specific residues. This method led to the identification of four main clusters and one outlier.

Cluster 1, which has the highest certainty (pLDDT = 90.3 ± 2.3), consists of models where the carbonyl of SF V625 alternates between turning inward and outward, i.e. toward and away from the central axis, among different subunits. Cluster 2 (pLDDT = 85.2 ± 1.6) is fairly similar, but the carbonyl of SF V625 is now flipped outward from the central axis in all subunits in most instances, and there is a noticeable constriction between G626 carbonyls. Cluster 3 (pLDDT = 77.5 ± 2.5) features the carbonyl reorientation of SF G626 and occasionally F627. In most models from these groups, the S6 helix rotates to varying extents, causing Y652 and particularly F656 side chains to rotate along and extending further into the hERG inner cavity. Both cluster 4 and the outlier cluster have low average pLDDTs (<70), rendering them unreliable for our analysis.

Intriguingly, while modeling hERG inactivation, we found that the SF conformations predicted by AlphaFold coincide with proposed hERG C-type inactivation mechanisms as highlighted in other experimental and computational studies(15, 26, 27). This correlation is particularly notable considering the structures in the mentioned studies have not been published in any publicly accessible databases, to the best of our knowledge. Specifically, the behavior observed in clusters 1 and 2, namely the flipping of V625 and the constriction at G626 carbonyls, was previously reported in a preprint study by Lau *et al*.(26, 27) Moreover, Li *et al.*'s computational work revealed an asymmetric SF conformation, where two opposing subunits exhibited similar V625 flipping and G626 narrowing as seen in our AlphaFold-predicted clusters 1 and 2, while the other two subunits displayed the G626 and F627 carbonyl reorientation characteristic of our cluster 3.(15) For our investigation, we chose to focus on the conformations seen in clusters 1 and 2, as this behavior was observed in both previous studies. We proceeded with further analysis and simulations using the best model from cluster 2, where all subunits consistently show the flipping of V625 carbonyls and pinching between G626 carbonyls.

Open-state clusters: In a control study, we used the conductive SF from the presumed open-state cryo-EM hERG structure (PDB 5VA2(7)), combined with the VSD and cytosolic domain, as the structural template for AlphaFold. Remarkably, the generated models converged almost uniformly into a single cluster, exhibiting negligible variance in both pLDDT and RMSD values across the models. The highest scoring model closely mirrors the experimental structure with reconstructed loops, showing only 0.5 Å all-atom RMSD due to minor differences in the loop conformations.

Comparison of state-specific hERG channel models

We refined the preliminary atomistic structural models putatively representing each functional state of the hERG channel (open, inactivated and closed) using Rosetta(25, 28) with an implicit membrane to optimize each residue orientation and resolve any steric clashes. The resulting models are compared in **Figure 3**. In **Figure 3a, b**, the closed-state model displays the most constricted channel pore, followed by the inactivated-state and then the open-state model. In the pore-lining S6 helix, the drug-binding residue Y652 maintains a consistent position in both closed and open hERG channel models. However, in the inactivated-state model, Y652 and its aromatic ring move slightly due to the rotation of the S6 helix, and together with the rotation of S624 sidechain hydroxyl oxygen away from the pore help form a shallow hydrophobic pocket above Y652 rings and beneath the SF. The rotation and movement of the pore-lining S6 helix also influences the position of residue F656 across the models, with its side chain protruding most into hERG inner cavity in the closed state, followed by the inactivated state and least in the open state.

Shown in **Figure S1a, b**, the SFs of the open- and closed-state models display similar arrangements, with carbonyl oxygens along the ion path all oriented inward to the central axis as in other K^+ channel structures, e.g., KcsA and K_V1.2, enabling efficient knock-on K^+ conduction(29, 30). In contrast, the inactivated-state model SF is distinct, marked by the lateral rotation of the V625 backbone carbonyl away from the central axis (**Figure S1c**), thereby creating a potential barrier preventing ion crossing from the S3 to S2 binding sites. Additionally, we noted a constriction between the G626 backbone carbonyls and a repositioning of the S624 sidechain hydroxyl oxygen. In the model representing the inactivated state, the carbonyl oxygens of G628 and F627 exhibit an upward shift relative to their positions in the open-state model. **Figure S1d-f** presents the SF of all three models from an extracellular perspective. In both the closed- and inactivated-state models, the F627 side chain undergoes a clockwise rotation when contrasted with its orientation in the open state. This rotational behavior aligns with findings from prior simulation study(14) where it was noted in a metastable non-conductive state. The loop that links the upper SF to the S6 helix rotates anti-clockwise relative to its position in the open-state model, consequently narrowing the upper part of the SF.

Echoing our observations, Lau *et al*., in a preprint, have suggested that the observed flipping of V625 carbonyls might be a potential C-type inactivation mechanism for the hERG channel(26, 27). Their study involved altering the external K^+ concentration to predispose the channels towards a non-conductive, inactivated-like state(26, 27). Li *et al.* made a similar observation in their study, demonstrating the constriction between G626 carbonyls which occurs asymmetrically in only two opposing subunits and not in the others to be a potential C-type inactivation mechanism(15). Indeed, this constriction was accompanied by the flipping of V625 carbonyls in the same subunits where the constriction was observed(15). Both structural features, which are also replicated in the AlphaFold-predicted model, might collectively constitute components of the inactivation mechanism.

Furthermore, Cuello *et al.* in their study of KcsA channel identified a similar constriction at G77 within the SF and a corresponding reorientation of the V76 carbonyl, resulting in a dilation in the SF at this location and correspondingly the loss of the S2 and S3 ion binding sites(31). Consequently, they suggested this backbone rearrangement as a fundamental molecular mechanism underlying C-type inactivation in K^+ channels(31). In other studies on Shaker and $K_v1.3$ channels, dilation in the upper SF has been proposed to be a potential C-type inactivation mechanism but without notable constriction at the SF glycine(32–35). The inactivation processes across various K+ channels may exhibit similarities to some degree, but possess distinct differences that could account for the observed variability in inactivation rates among different K+ channels(1).

For the VSD, we measured the distances between the backbone C_α atoms of the gating charge residues (K525, R528, R531, R534, R537, K538) on the S4 helix and the gating charge transfer center F463 on the S2 helix, as shown in **Figure 3c**. Although we observed an increased distance between the gating charge residues and the charge transfer center residue in the closed state, this separation was not due to a straight downward movement of the S4 helix. Instead, the closed-state model S4 exhibited a minor kink around residue R531 and lateral movement toward the center of the channel, impacting the S4 – S5 linker and consequently nudging the S5 helix inward, effectively narrowing the pore. It should be emphasized that the predicted closed-state model exhibits lower confidence levels for the S4 helix and S4-S5 linker residues (pLDDT ≤ 75) when compared to their counterparts in models of other states, necessitating caution in interpreting the physiological implications of this observation. Conversely, the pore region, which demonstrates closure, is characterized by a higher prediction confidence (pLDDT ≥ 75), suggests a more robust and reliable representation in this part of the model. **Supporting Movie 1** is showcasing the morph between each hERG channel model.

In **Figure 4a** and **b**, we analyzed interactions of extracellular S5-P linker (I583 – Q592) along with SF and surrounding SF residues (S620 – N633) through heatmaps detailing hydrogen bonding, π stacking, cation-π, and salt bridge formation similarities and differences (**Table S1** shows detection criteria; distance-based contact maps(36) for all residues are shown in **Figure S2**). Distinct interaction patterns between open- and inactivated-state models were observed in these regions (**Figure 4b, c**). N633 atop the SF forms hydrogen bonds with S5-P linker G584 and Q592 from an adjacent subunit, while N629 forms hydrogen bonds with adjacent S631. Additionally, SF G626 forms a hydrogen bond with S620 behind the SF. Within the S5-P linker, N588 and D591 also display hydrogen bonding. However, these stabilizing interactions in the open-state model SF region are absent in the inactivated-state model, where only intra-subunit hydrogen bonds between I583 (S5-P linker) and N633 (SF) occur, along with V630 bonding with N629 atop the SF.

To corroborate our findings, mutations involving the residues above have been shown to impact hERG inactivation as evidenced in numerous clinical and experimental studies(14, 37–44). For instance, the S631A mutation, linked to short QT syndrome, causes a positive shift in hERG half-inactivation voltage(38), while S631C speeds up fast inactivation(39). N629D, N629S, and N633S mutations, found in long QT syndrome patients, disrupt inactivation and K^+ selectivity (14, 40). N588K/E and Q592K modulate rapid inactivation(41, 42), G584S leads to inactivation gating defects(45), and S620T abolishes hERG inactivation(43). V630L caused a negative shift in the voltage dependence of steady-state inactivation(44), while H587P/K disrupts the C-type inactivation process and K^+ selectivity(37). N588C and I583C mutations have high and intermediate impact of hERG inactivation(46). Lastly, the D591R/Q592R double mutation inhibits inactivation(42).

There are fewer differences between the open- and closed-state models (**Figure 4b, d**). In the open-state model, D591 from the S5-P linker forms hydrogen bonds with N588, and G584 bonds with N633 at the top of the SF. These interactions are absent in the closed-state model, where H587 (instead of N588) bonds with D591 within the S5-P linker, and I583 (replacing G584) interacts with N633 at the SF top. Additionally, G628 from an adjacent subunit forms a hydrogen bond with N629 atop the SF. Analyzing the differences between the inactivated- and closed-state model (**Figure 4e**), the inactivated-state model uniquely features a V630-N629 hydrogen bond, whereas the closed-state model exhibits intersubunit hydrogen bonds between N633 and Q592, and between S631/G628 and N629. Furthermore, in the closed-state model, S620 forms a hydrogen bond with G626, stabilizing the SF conformation.

In **Figure S3**, we compared the S6 pore-lining helix orientation across various models. The closed-state model features a straight S6 helix with a minor kink. On the contrary, both the open- and inactivated-state models exhibit a pronounced kink around I655, as identified in a prior study(47), which facilitates pore opening and distinguishes the inactivated-state from the closed-state model. Notably, a slight rotation differentiates the S6 helix in the open- and inactivated-state models, altering the alignment of drug-binding residues Y652 and F656. The interaction network analysis results from **Figure 4b, c** suggest that alterations in the hydrogen bond network around the SF region, during the transition from open to inactivated state, might pull on the S6 helix and influence its orientation (**Figure S1e, f**) – a subtle yet potentially impactful change for drug binding which we will explore later. In agreement with our observations, a study by Helliwell *et al.* also suggested that a slight clockwise rotation of the S6 helix in the hERG open-state cryo-EM structure(7) could align the S6 aromatic side chains, particularly F656, into a configuration to enable interactions with inactivation-dependent blockers that more accurately reflects experimental data(48).

Molecular dynamics simulations to assess ion conductivity

We performed all-atom molecular dynamics (MD) simulations on two hERG channel models described above, one in the open state and the other in the predicted inactivated state, to evaluate their ion conduction capabilities. Unlike the closed-state model, both open- and inactivated-state models should allow ions and water to enter and traverse the channel pore reaching the SF region. However, only the open state-model is expected to facilitate ion conduction through its SF.

To investigate ion conduction in the selectivity filter, we considered two conditions, as shown in **Figure 5a**: one in which the SF initially contained only K^+ ions and another in which both ions and water were present to test previously proposed direct (or Coulombic) and water-mediated K^+ conduction knock-on mechanisms(49, 50) as in a previous study(14). In the direct knock-on (ions-only) scenario, we manually positioned K^+ atoms in the putative K^+ binding sites of S0, S2, S3, and S4 within the SF. For water-mediated knock-on (the alternating ions and water molecules) scenario, K^+ ions were placed in the S1, S3, and S_{cav} positions, while water molecules were inserted into the S0, S2, and S4 positions. These models were incorporated into phospholipid bilayers consisting of *1-palmitoyl-2-oleoylphosphatidylcholine* (POPC) molecules, as depicted in **Figure 5b**. Subsequently, we conducted simulations for each case under three membrane voltage conditions: 0 mV, 500 mV, and 750 mV, each lasting 1 µs. This resulted in a total of six MD simulations for each model.

For all instances where a non-zero membrane voltage was applied, we observed K^+ conduction after equilibration in the open-state model (**Figure 6a, c** and **Figure S4a, c**), whereas such conduction was not observed in the inactivated-state model (**Figure 6b, d** and **Figure S4b, d**). For ions-only initial arrangement we observed that all K^+ ions initially located in the SF went across during 1 µs MD runs under applied 750 and 500 mV membrane voltage (**Figure 6a** and **Figure S4a**), whereas for the alternating water-ion initial SF configuration we observed conduction of SF ions as well as additional K^+ moving all the way across the channel pore (**Figure 6c** and **Figure S4c**). In both cases we saw combination of direct and water-mediated knock-on mechanisms as in our previous hERG channel MD simulations(11, 14). Control MD simulations conducted under zero voltage conditions revealed a single K^+

conduction event for the open-state model (**Figure S4g**) when the SF was initially filled with water molecules and ions, while no conduction events were observed in the remaining cases (**Figure S4e, f, h**).

Subsequently, we conducted an analysis of pore radius changes throughout the MD simulations (full results in **Figure S5**). In **Figure 7a**, under zero voltage conditions, we observed consistent and distinct pore radius profiles across all simulations within their respective models. Specifically, MD simulations featuring the inactivated-state model consistently displayed a narrower pore radius when compared to simulations involving the open-state model. However, when subjected to high voltage conditions, the open-state model exhibited a shift towards an inactivated-like state, leading to a reduction in the pore width, which is consistent with an increased hERG channel inactivation propensity at more depolarized voltages(1). Although we did not observe the outward flipping of the V625 backbone carbonyl oxygens in the SF during the 1 μs simulations of the open-state model, we did observe the flipping of the F627 backbone carbonyl oxygens as shown in **Figure 7b**. Interestingly, this SF conformation with flipped F627 but not V625 backbone carbonyls is also observed in cluster 3 of the AlphaFold-predicted models shown in **Figure 2**. In the inactivated-state model MD simulations, V625 backbone carbonyl oxygens flipped inward into ion conducting conformation more often with increasing voltage, but as long as one out of four of them remained outward oriented, no K^+ could pass through the SF.

Assessing state-dependent drug block using GALigandDock

We utilized Rosetta GALigandDock software(13) to dock 19 drugs from different classes, including alternative protonation states, into our hERG state-specific channel models. This process aimed to evaluate and corroborate their state-dependent binding interactions with experimental studies, specifically in terms of relative binding affinities. **Figure 8** presents these findings in the form of Rosetta GALigandDock(13) binding energies (lower values mean more favorable binding). Consistent with published studies, most drugs showed stronger binding to the inactivated-state hERG channel model, including astemizole(8), terfenadine(8), cisapride(8), d/l-sotalol(8), dofetilide(8), and E-4031(51, 52). Drugs like moxifloxacin(53), quinidine(8), and perhexiline(8) did not show strong preference for the inactivated model, aligning with findings from hERG experimental studies using inactivation-deficient mutants(8) or “step-ramp” voltage protocol(53).

In our GALigandDock docking results, most drugs exhibited increased binding affinity to the closed-state hERG model compared to the open-state hERG model. Drugs are unable to bind to the closed state from the intracellular space because the pore is closed. However, they can become trapped if they are already bound when the channel transitions from open to closed state, as shown in experiments for dofetilide(54), cisapride(54), terfenadine(54, 55), E-4031(55), nifekalant(56), etc. To model drug trapping, we placed the drug in a pocket beneath the selectivity filter in the closed pore configuration before docking. However, this method does not consider how the conformational shift from the open to the closed state might influence drug binding. Under physiological conditions, the pore gating motion from open to closed might expel drugs from the pore instead of pushing them deeper. This limitation might account for some inconsistencies noted in our docking study, particularly regarding the apparent trapping of drugs such as amiodarone and haloperidol, which is at odds with experimental results(57). However, these preliminary results could pave the way for more thorough investigations, employing advanced computational techniques to delve deeper into the dynamics of drug trapping(58, 59).

In most cases, the increased drug binding affinity to the inactivated-state hERG model can be attributed to the protrusion of residue F656 aromatic side chain into hERG central cavity (**Figure 3a**). This protrusion has the potential to strengthen drug binding through providing extra π stacking or hydrophobic interactions. Furthermore, the side chains of F656 could act as a barrier, blocking drugs that are bound deeper within the pore from escaping even when they do not have direct interactions with the drugs. Similar observations were made for the closed-state model, where the pore closure also positions the F656 side chain inward. In addition, the slanted orientation of the Y652 aromatic ring and repositioning of the S624 sidechain hydroxyl oxygen in the inactivated model enabled the formation of a pocket beneath the SF (**Figure 3b**), enabling drugs to reach deeper into the pore.

As an example,

Figure 9 focuses closely on the binding of astemizole, dofetilide, and quinidine in their cationic forms (the predominant species at the physiological pH 7.4) to different hERG channel models. Experimental evidence(8) suggests that dofetilide and astemizole bind more potently to the inactivated state, while quinidine does not exhibit this preference.

Astemizole: In the open-state model, astemizole engages in π stacking with the Y652 aromatic side chain via its benzimidazole group and forms hydrophobic contacts with adjacent residues (A653, F656, and Y652). Its binding occurs just below S6 helix residue Y652, not deeply within the pore, resulting in a binding pocket that remains partially open to external solvent. In contrast, in the inactivated-state model, astemizole demonstrates an increase in interactions and becomes fully enclosed within the binding site deeper into the pore, engaging in hydrophobic interactions with S6 residues S649, Y652, F656, I655 and S5 residue F557. Astemizole phenyl ether group engages in the π stacking with hERG Y652 and F656 side chains from adjacent subunits. At the other end, the aromatic ring of Y652 phenol side chain also engages in π stacking, while its oxygen atom acts as a non-ideal hydrogen bond acceptor (i.e., donor angle of ≤ 45° and bonding distance of ≤ 3.8 Å(60)) to astemizole nitrogen. Furthermore, the SF residue S624 side chain participates as a hydrogen bond acceptor with the piperidine ring of the drug. The binding pattern in the closed-state model is similar to that in the inactivated-state model, but it includes additional hydrophobic interaction with S660 and an extra hydrogen bond provided by the phenol oxygen of Y652.

In 2021, a study by Asai *et al.* solved the cryo-EM hERG structure in complex with astemizole(10). Although the structures deposited to the PDB (7CN0(10) and 7CN1(10)) did not depict any bound ligand, a possible astemizole binding pose was suggested based on residual EM density. The density map showed a π-π interaction of astemizole with Y652 and a hydrogen bond with S624(10). In addition, electrophysiology study by Saxena *et al.* has identified F557 and Y652 as crucial for astemizole binding, as determined through mutagenesis(61). In 2022, a study by Nano Imaging Services unveiled a cryo-EM structure of hERG with astemizole at a refined 2.7 Å resolution(62), showcasing a binding pose remarkably similar to what we observed in our study for the hERG inactivated state.

Dofetilide: In the open-state hERG model, dofetilide interacts with multiple residues of the pore lining S6 helices. For instance, it forms hydrogen bonds with two S660 residues from opposite subunits and two A653 residues from adjacent subunits. Additionally, there are hydrophobic interactions with Y652 and G657. When bound to the inactivated-state model, dofetilide settles deeper into the pore, extending horizontally above the Y652 residue, where it forms π stacking and cation-π interactions, as well as hydrogen bonds with the Y652 residues of all subunits. The backbone carbonyl oxygen of residue S649 also engages in hydrogen bonding with the nitrogen in the sulfonamide group of dofetilide. There are also hydrophobic contacts with hERG S6 residues S649, F656, and I655 as well as residue F557 on the S5 helix. The closed-state model pore provides a substantially narrower space, leading dofetilide to bind vertically along the pore axis, forming hydrophobic contacts with S624, S649, Y652, F656, and S660. Here, the oxygen and nitrogen of its sulfonamide group create a series of hydrogen bonds with hERG residues T623 and Y652. The central cationic ammonium group of the ligand forms cation-π interactions with two F656 residues from adjacent subunits. Lastly, the oxygens in the remaining sulfonamide group are involved in hydrogen bonding with the S660 residues from every subunit. In the inactivated-state and closed-state models, the binding pocket is completely enclosed, notably unlike the open-state model.

In line with our results, mutations affecting A653 have demonstrated an influence on hERG channel blocking by dofetilide(63). Additionally, electrophysiology study by Saxena *et al.* revealed that mutants Y652A and F557 altered dofetilide binding(61). Simulation studies have highlighted interactions involving non-polar residues A653, Y652, F656, as well as polar residues S624, T623, S649, and S660 with dofetilide(64).

Quinidine: Unlike the previous two drugs, quinidine does not exhibit significant state-specific binding based on our docking predictions (**Figure 8**). In the open-state hERG model, its small size allows for complete enclosure within the binding pocket, where it forms non-ideal hydrogen bonds with residue Y652 and hydrophobic contacts with another Y652 from an adjacent chain as well as A653 and S660. In the inactivated-state model, quinidine binds lower in the pore, resulting in a partially open binding pocket. Here, its quinoline rings engage in π-stacking interactions with the F656 side chain above and hydrophobic contacts with another F656 from the opposite subunit. The hydroxyl oxygen forms a non-ideal hydrogen bond with residue S660. In the closed-state model, quinidine becomes trapped deeper in the pore and is fully enclosed. Its quinoline rings π stack with multiple F656 side chains below and the Y652 side chain above drug binding position. The hydroxyl oxygen now establishes a non-ideal hydrogen bond with Y652, with additional hydrophobic contacts observed with Y652 side chains and the T623 backbone. Corroborating our results, Sǎnchez-Chapula *et al.* previously found that mutating key aromatic residues (Y652, F656) in the S6 domain reduced the efficacy of quinidine by more than 100-fold(65).

Conclusions

Employing AlphaFold2 under default parameters typically leads to the prediction of the hERG channel in the open-state conformations. In our study, we presented an approach to guide AlphaFold2 to model the hERG channel in various conformational states. We further validated the physiological significance of these states using computational simulations. This methodology has provided new insights into the structural and functional behavior of the hERG channel, including state-specific drug interaction mechanisms.

The predicted models, which putatively represent the closed, open and inactivated states of the hERG channel, have revealed detailed structural aspects that were previously elusive, particularly in the pore region where drug binding occurs. The closed-state hERG channel model demonstrates a constricted pore and deactivated voltage-sensing domains, suggesting a structural basis for the prevention of ion passage. The open-state hERG channel model, conversely, illustrates a pore conformation accessible to ion conduction, aligning with the physiological role of the channel in cardiac repolarization. The inactivated-state hERG channel model, a prediction of which greatly contributes to our understanding to hERG channel gating mechanism, shows a non-conductive selectivity filter conformation with significant changes to the pore region that could be a key in understanding state-specific drug-induced channel blockade. The non-conductive SF predicted by AlphaFold2, characterized by flipping of SF V625 carbonyl oxygens away from the central axis and minor constriction at the level of G626, aligns with prior computational analyses and preliminary experimental reports as a possible hERG C-type inactivation mechanism(15, 26, 27). The structures referenced in these studies have not been published in any publicly available databases and used for the training of AlphaFold2 to our knowledge. Our approach thus underscores the substantial yet untapped potential of AlphaFold2 to predict *de novo* channel conformations with physiological relevance.

Molecular dynamics simulations were crucial in confirming these model functional properties. The observed differences in ion conduction between the open and inactivated hERG channel states illustrate the impact of structural changes on ion channel activity. In addition, the drug docking analysis matched expectations, with significant preference for the inactivated-state model across a variety of hERG blockers. In the model representing the inactivated state, a subtle rotation of the S6 pore-lining helix from the open state results in a more prominent protrusion of the F656 side chains into the central cavity and widens the inner cavity below the SF due to the repositioning of Y652 side chains. These structural modifications facilitate deeper binding of certain drugs in the pore, increase interactions between drugs and the channel, impede ion movement, and obstruct the exit routes for drugs that are bound within the pore. Although prior studies have proposed potential molecular mechanisms for hERG C-type inactivation(15, 26, 27), they have primarily concentrated on conformational shifts leading to a non-conductive selectivity filter. Our research, however, also sheds light on how these alterations extend to the pore region and subsequently impact drug binding, an issue of significant relevance in safety pharmacology and drug development.

Moreover, the study highlights the potential for deep-learning based computational methods like AlphaFold2 in structural biology, especially for complex proteins like ion channels and a simultaneous prediction of multiple conformations putatively representing different channel states. This is a challenging task for experimental structure determination as it requires changes in experimental conditions and/or classification of multiple cryo-EM images. Our proposed AlphaFold2 approach using multiple templates and fine-tuned structural prediction parameters allowed us to overcome this challenge and predict atomistic structural models of the hERG channel in the putative closed, open, and inactivated states. These models were further validated using all-atom molecular dynamics simulations under applied voltage to test ion conduction through model channel pores as well as molecular docking of multiple drugs to test their state-dependent binding preferences compared to known experimental data. The intersection of structural modeling, molecular docking and molecular dynamics simulations, and supporting experimental data offers a comprehensive approach to understanding protein structures and their links to biological functions.

Despite the promising results, our study is not without limitations. While AlphaFold has demonstrated remarkable accuracy in numerous instances(66–68), it is important to note that the predicted models, particularly in regions where the model has lower confidence, may not always be reliably accurate to predict drug binding poses(69). Moreover, hERG channel inactivation and closure might encompass a range of states, and the conformations we have identified could potentially represent just a few possibilities within this broad spectrum. The results from GALigandDock drug docking, while providing valuable insights, should be regarded as provisional due to inherent limitations of this approach, including limited accuracy and transferability(19). Additionally, knowing the computational binding free energies of a drug is not the complete story; binding rates such as k_{on} (association rate) and k_{off} (dissociation rate) are also crucial for a quantitative evaluation of drug binding to the channel. The results herein primarily serve as a basis for further detailed investigation using methods like molecular dynamics simulations linked to multiscale functional modeling, as demonstrated in previous studies(11, 70).

In conclusion, this study not only advances our knowledge of the hERG channel structural dynamics but also sets a precedent for using AlphaFold2 or similar computational methods, such as RoseTTAFold(71), to study other ion channels and membrane proteins. The insights gained from this study are expected to have a lasting impact on the fields of ion channel physiology and pharmacology including cardiac drug safety, providing a foundation for future research aimed at developing safer and more effective therapeutic agents.

Methods

hERG channel model generation and refinement

Structural data for the Eag K_V channel in its closed conformation (PDB 8EP1(21)) and the hERG channel in its open state (PDB 5VA2(7)) were sourced from the Protein Data Bank (PDB(72)). To accurately represent the open state of hERG, we integrated known cryo-EM structures (PDB 5VA2(7)) with modeled segments of absent loops, employing Rosetta(28) software suite LoopRemodel mover in a symmetrical configuration. The refinement of all final models was performed using Rosetta FastRelax protocol, which iterated 15 times and included a simulated POPC membrane environment. For each finalized model, 10 separate relaxation runs were executed, and the highest-scoring model from these runs was selected for further simulation and analysis.

Cloud computational resources, specifically NVIDIA A10 GPUs (24 GB of VRAM) provided by Oracle, facilitated the modeling processes in ColabFold(22). To enhance sampling diversity, in each modeling session, ColabFold was configured to utilize 256 sequence clusters and 512 extra sequences (*max_msa* = *"256:512"*) under the MSA option and have dropouts enabled (*use_dropout* = True). The prediction phase was further diversified by running 20 iterations with different random seeds (*num_seeds* = 20), each producing 5 models and resulting in 100 total models per run. An exception to this approach was the initial phase of inactivated-state hERG model creation, where a single seed number was used to generate 5 models. The number of iteration cycles was set to 20, with an early stopping tolerance of 0.5 based on per-residue confidence metric pLDDT deviation from the previous cycle.

Atomistic MD simulations of hERG channel conduction

The CHARMM-GUI web server(73) was employed to embed hERG channel structural models within tetragonal patches of phospholipid bilayers, each comprising approximately 230 to 240 POPC lipid molecules. The resulting assemblies were immersed in a 0.3 M KCl aqueous solution, culminating in molecular systems with an approximate total of 144,000 atoms. Residue protonation states were determined assuming a neutral pH environment, and each channel subunit was terminated with standard charged N- and C-termini.

MD simulations were conducted using the Amber22(74) software suite. The simulations utilized standard all-atom CHARMM force fields specific to proteins (CHARMM36m(75)), lipids (C36(76)), and ions, in conjunction with the TIP3P water model(77). The systems were maintained at 310.15 K and 1 atm pressure in the isobaric-isothermal (*NPT*) ensemble, facilitated by Langevin temperature equilibration and the Berendsen barostat. Non-bonded interactions were calculated with a cutoff of 12 Å. Long-range electrostatic forces were addressed using the Particle Mesh Ewald (PME) method(78), and van der Waals interactions were not subjected to long-range correction as per recommendations for the C36 lipid force field. All hydrogen-involved covalent bonds were constrained using the SHAKE algorithm to enable a 2-fs MD simulation time step.

Equilibration began with harmonic restraints imposed on protein atoms and lipid dihedral angles, initially set at 20 kcal/mol/Å² and reduced to 2.5 kcal/mol/Å² over 6 ns. A subsequent 90 ns equilibration phase further decreased the restraints to 0.1 kcal/mol/Å², initially encompassing all atoms in the protein and eventually focusing solely on the backbone atoms of pore-lining residues (G546 to F720). In selected MD simulations, an electric field was applied along the Z direction to mimic membrane voltage, increasing linearly over the final 10 ns of equilibration to reach either 500 or 750 mV. This setup prefaced a production phase lasting 910 ns, totaling 1 μs of total simulation time per each case.

Docking of drugs to hERG channel models

Ligand structures (i.e., pharmaceutical compounds) were retrieved from the PubChem(79) and ZINC(80) databases. Afterward, each ligand underwent modification processes including bond corrections and setting of protonation states using the Avogadro software(81). In this study, we considered the protonation state of the top two most dominant species at the physiological pH of 7.4, computed using the Henderson–Hasselbalch equation. After these initial modifications, each ligand partial atomic charges, as well as atom and bond types, were refined using AM1-BCC correction via the Antechamber module in AmberTools22(74, 82).

Each ligand was individually positioned within the pore of the hERG channel, specifically between the key drug-binding residues, Y652 and F656, located on the pore lining S6 helices. This manual placement was a preparatory step for the docking process. Docking was executed using the GALigandDock(13) Rosetta mover, a component of the Rosetta software suite(28). The *DockFlex* mode was utilized for this purpose with a spatial padding of 5 Å. For every individual hERG channel – ligand pair, a total of 20 parallel runs were conducted. Each run generated 1,250 unique docking poses, cumulatively providing a substantial collection of 25,000 poses for each ligand – hERG channel complex. This extensive array of poses was intended to ensure a comprehensive exploration of potential ligand binding configurations and orientations within the hERG channel pore.

Utilizing in-house Python scripts, we selected the top 50 docking poses for each ligand based on the lowest free energy of binding as calculated by GALigandDock. These selected poses were then clustered based on ligand all-atom RMSD, factoring in the symmetry of the hERG channel to ensure accurate grouping. The clustering was executed with an RMSD threshold of 2.5 Å, and only clusters containing a minimum of 8 poses were deemed significant; those with fewer were classified as outliers. Within the cluster with the most favorable average binding free energy, we selected the top scoring pose as the representative pose for further analysis. This pose was then subjected to a detailed analysis of protein-ligand interactions utilizing the Grapheme Toolkit from the OpenEye software suite(83). The criteria for detecting interactions are outlined in the OEChem Toolkit manual(60), with two modifications: the *MaxContactFraction* is set to 1 (default: 1.2), and the *MaxCationPiAngle* is adjusted to 30° (default: 40°). The interaction patterns and binding sites were subsequently rendered as a two-dimensional image for comprehensive visual interpretation. Additionally, for a more detailed understanding of the spatial arrangement, three-dimensional visualization of the protein-ligand complexes was conducted using the ChimeraX[20] software.

Molecular graphics and interaction analysis

Molecular graphics visualization was performed using ChimeraX(84). MD trajectory and simulation images were visualized using VMD(85). Interaction network analysis was performed using the Protein-Ligand Interaction Profiler(86) with criteria outlined in **Table S1**.

Acknowledgments

We would like to thank all members of the I.V., C.E.C. and V.Y.-Y. laboratories and the cats, Momo and Mimi, for helpful discussions and support. This work was supported by National Institutes of Health Common Fund Grant OT2OD026580 (to C.E.C. and I.V.), National Heart, Lung, and Blood Institute (NHLBI) grants R01HL128537, R01HL152681, and U01HL126273 (to C.E.C., V.Y.-Y. and I.V.), American Heart Association Career Development Award grant 19CDA34770101 (to I.V.), National Science Foundation travel grant 2032486 (to I.V.), UC Davis

Department of Physiology and Membrane Biology Research Partnership Fund (to C.E.C. and I.V.) as well as UC Davis T32 Predoctoral Training in Basic and Translational Cardiovascular Medicine fellowship supported in part by NHLBI Institutional Training Grant T32HL086350 (to K.N.). Computer allocations were provided through Extreme Science and Engineering Discovery Environment (XSEDE) grant MCB170095 (to I.V., C.E.C., and V.Y.-Y.), Texas Advanced Computing Center (TACC) Leadership Resource and Pathways Allocations MCB20010 (I.V., C.E.C., and V.Y.-Y.), Oracle for Research fellowship and cloud credits award (to I.V., C.E.C.), Pittsburgh Supercomputing Center (PSC) Anton 2 allocations PSCA17085P, MCB160089P, PSCA18077P, PSCA17085P, PSCA16108P (to I.V., C.E.C., and V.Y.-Y.). Anton 2 computer time was provided by the Pittsburgh Supercomputing Center (PSC) through Grant R01GM116961 from the National Institutes of Health. The Anton 2 machine at PSC was generously made available by D.E. Shaw Research. OpenEye academic license was provided by OpenEye Scientific.

Data availability

The data that support the findings of this study are available from the corresponding authors upon request.

Ethics declarations

Competing interests: The authors declare no competing interests.

Figure captions

Figure 1. Generation of hERG channel models in the closed (a), open (b), and inactivated (c) states. The lower limit of the pore radius color profile (1.15 Å) indicates the minimum radius to accommodate a water molecule, and the upper limit (2.30 Å) indicates sufficient space to fit two water molecules side by side.

Figure 2. Clustering of AlphaFold2-predicted hERG channel models. a) The model chosen for subsequent analysis**. b)** Clusters created from 100 models predicted for each state. Each structure visualized is colored according to the per-residue confidence metric (pLDDT). The closed-state models are clustered based on the RMSD of the entire protein models. The inactivated- and open-state models are clustered based on the RMSD of the selectivity filter (S624 – G628). To represent each cluster, the top 5 models ranked by average pLDDT are shown. The bar graphs display the mean pLDDT values for the clustered segment across all models within each cluster, accompanied by the standard deviation. Clusters containing less than three models are categorized as outliers.

Figure 3. Structural comparison of different hERG channel state models. a) Visual comparison of the closed, open-, and inactivated-state models. **b)** Pore radius for the SF and drug binding region (upper) and for the entire pore (lower). **c)** Comparison of the VSD conformation in each model, showcasing the positively charged Arg and Lys gating-charge residues, located on the S4 helix, and the gating charge transfer center residue, F463, on the S2 helix. **d)** Measurement of the distance between the C_α atom of F463 to the C_α atom of each of the gating-charge residues.

Figure 4. Interaction network analysis showcasing residue-residue interactions in the S5-P linker (I583 – Q592) and region surrounding the SF (S620 – N633). a) An image of a hERG channel subunit with the analyzed regions colored in cyan and blue. **b)** Heatmaps showing intrasubunit and intersubunit (marked by X) interactions between each residue in the analyzed regions. The interactions analyzed are hydrogen bonding, π stacking, cation-π, and salt bridges. Black cells indicate no interactions. Gray cells indicate an interaction is present in both states. Blue, orange, and green colored cells indicate the interaction is present only in the open, inactivated, or closed state, respectively, but not in the other state being compared in the map. White lines are added to separate S5-P linker residues from the SF region residues. **c, d, e)** Visualization of the interactions being present in one state but not the other. Gold-colored residues are involved in the interactions. Green-colored residues, named with an asterisk at the end, are from an adjacent chain but are interacting with gold-colored residues. Dashed lines represent hydrogen bonds.

Figure 5. Setup of MD simulations to assess ion conduction in the open and inactivated models. a) Initial configuration of the SF, set to fill with either all K^+ ions, or alternating K^+ and water molecules. **b)** An example MD simulation box showing a hERG channel model (shown in yellow surface representation) embedded in POPC lipid

bilayer (shown as sticks) and solvated by an aqueous 0.3 M KCl solution (shown as a transparent surface with K^+ and Cl^- ions shown as purple and green balls, respectively).

Figure 6. Movement of K^+ ions through hERG SF. The *z* coordinates of K^+ ions are tracked as they traverse from the pore of the channel (lower *y*-axis limit) to the extracellular space (upper *y*-axis limit) under membrane voltage of 750 mV. Putative K^+ binding sites in the SF (S0 – S5) are marked using blue dashed lines in the plots. **a, c)** Results from MD simulations on the open model with the SF initially configured to have only K^+ ions or alternating K^+ / water molecules, respectively. **b, d)** Results from MD simulations on the inactivated model with the SF initially configured to have only K^+ ions or alternating K^+ / water molecules, respectively.

Figure 7. Analysis of dynamics of the SF and pore conformations over the course of the 1 µs MD simulations. a) Pore radius averaged over each 1 µs long MD simulations with or without applied membrane voltage. Open- and inactivated-state model MD simulations are notated as O and I, respectively, with the subscripts KK and WK denoting whether the SF initially configured to have only K^+ ions or alternating K^+ / water molecules, respectively. **b)** Ensembles of SF conformation over the course of each MD simulation superimposed over each other. The gold-colored conformation indicates the initial conformation.

Figure 8. GALigandDock drug docking results to different hERG channel models. Each bar plot represents the estimated energy of binding in Rosetta energy units (R.E.U.) for the named drug to the open-, inactivated-, and closed-state hERG channel models. Lower values mean more favorable binding. 25,000 docking poses were generated for each drug/channel model pairing. The top 50 poses were clustered, and the plotted energy represents the average free energy of the top cluster along with the standard deviation. The labels (0), (+), (±) after the drug name indicate its neutral, cationic, or zwitterionic form, respectively.

Figure 9. Visualization of interactions for cationic astemizole (a), dofetilide (b), and quinidine (c) to different hERG channel models. Each panel includes 3 subpanels showcasing drug interactions to the open-, inactivated, and closed-state hERG channel models. In each subpanel, an overview of where the drug binds within the channel pore is shown on the upper left, a 3D visualization of interactions between each channel residue (blue, red, green, and tan residues are from the subunit A, B, C, or D, respectively) to the drug (magenta) is shown on the upper right, and a 2D ligand – protein interaction map is shown at the bottom. A continuous gray line depicts the contour of the protein binding site, and any breaks in this line signal areas where the ligand is exposed to the solvent.

Figures and Tables

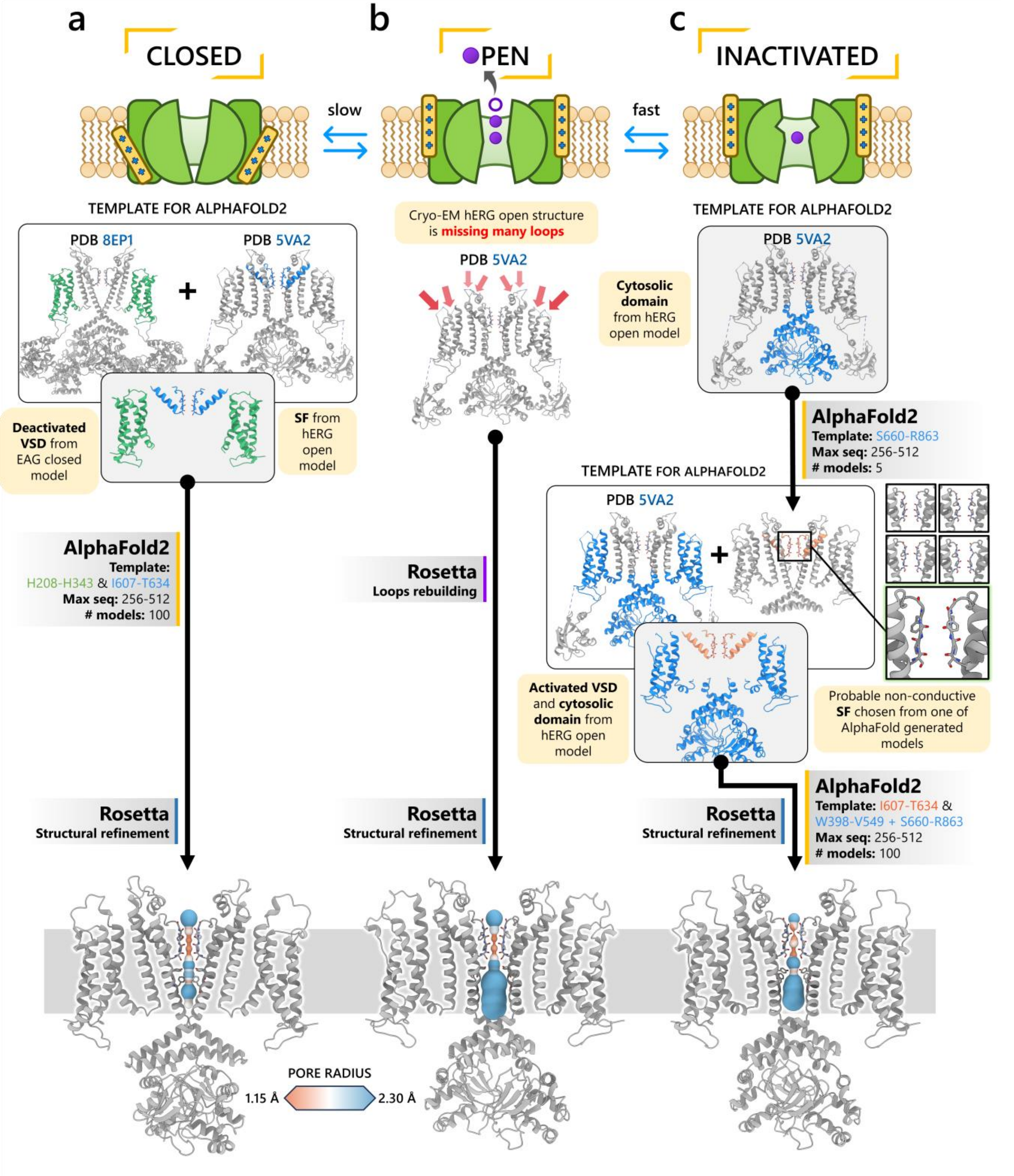
a
CLOSED
b
OPEN
c
INACTIVATED
slow
fast
TEMPLATE FOR ALPHAFOLD2
PDB 8EP1
+
PDB 5VA2
Deactivated VSD from EAG closed model
SF from hERG open model
Cryo-EM hERG open structure is missing many loops
PDB 5VA2
TEMPLATE FOR ALPHAFOLD2
PDB 5VA2
Cytosolic domain from hERG open model
AlphaFold2
Template: H208-H343 & I607-T634
Max seq: 256-512
# models: 100
Rosetta
Loops rebuilding
AlphaFold2
Template: S660-R863
Max seq: 256-512
# models: 5
TEMPLATE FOR ALPHAFOLD2
PDB 5VA2
+
Activated VSD and cytosolic domain from hERG open model
Probable non-conductive SF chosen from one of AlphaFold generated models
AlphaFold2
Template: I607-T634 & W398-V549 + S660-R863
Max seq: 256-512
# models: 100
Rosetta
Structural refinement
Rosetta
Structural refinement
Rosetta
Structural refinement
PORE RADIUS
1.15 Å
2.30 Å

Figure 1. Generation of hERG channel models in the closed (a), open (b), and inactivated (c) states. The lower limit of the pore radius color profile (1.15 Å) indicates the minimum radius to accommodate a water molecule, and the upper limit (2.30 Å) indicates sufficient space to fit two water molecules side by side.

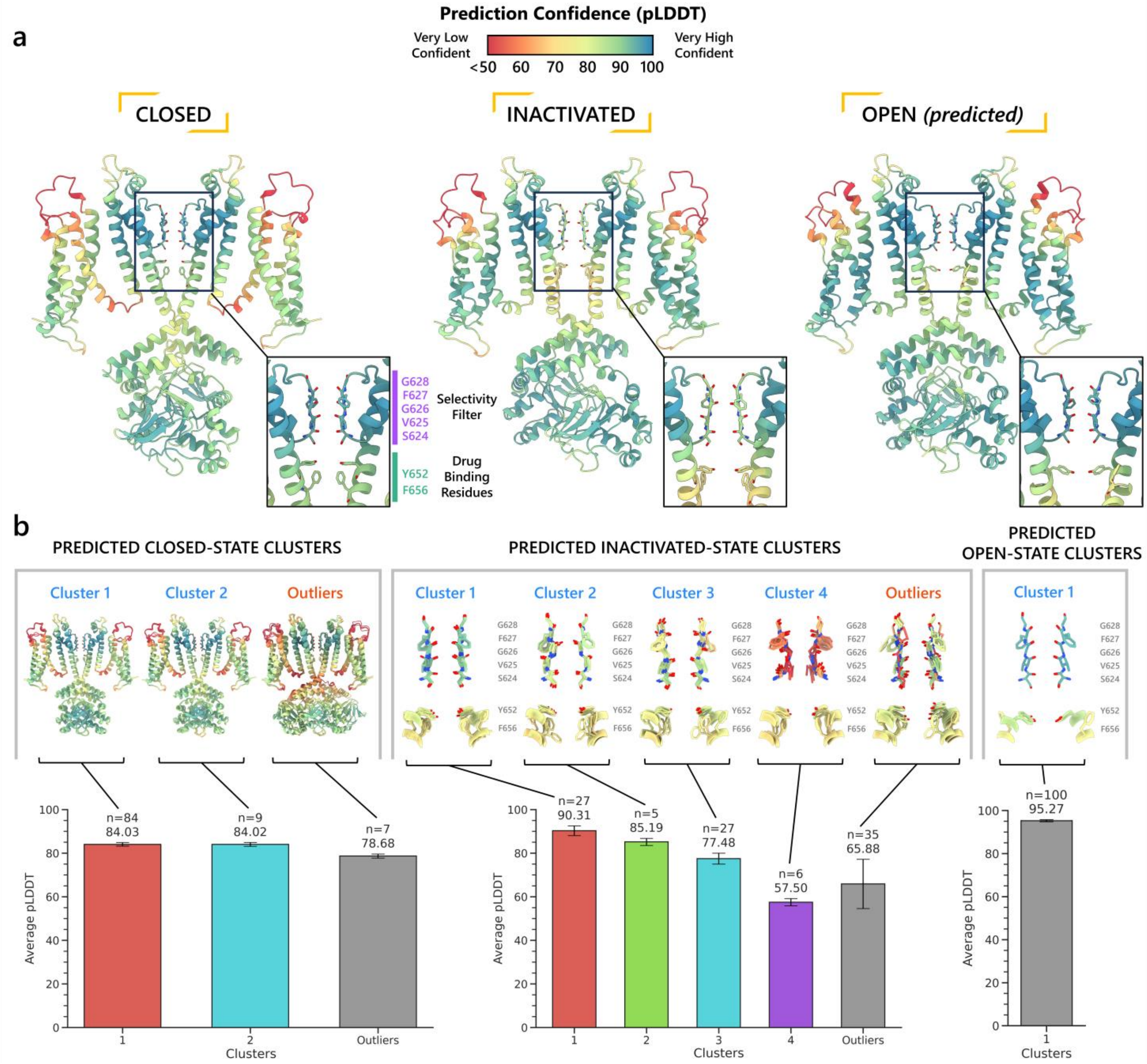

Figure 2. Clustering of AlphaFold2-predicted hERG channel models. a) The model chosen for subsequent analysis**. b)** Clusters created from 100 models predicted for each state. Each structure visualized is colored according to the per-residue confidence metric (pLDDT). The closed-state models are clustered based on the RMSD of the entire protein models. The inactivated- and open-state models are clustered based on the RMSD of the selectivity filter (S624 – G628). To represent each cluster, the top 5 models ranked by average pLDDT are shown. The bar graphs display the mean pLDDT values for the clustered segment across all models within each cluster, accompanied by the standard deviation. Clusters containing less than three models are categorized as outliers.

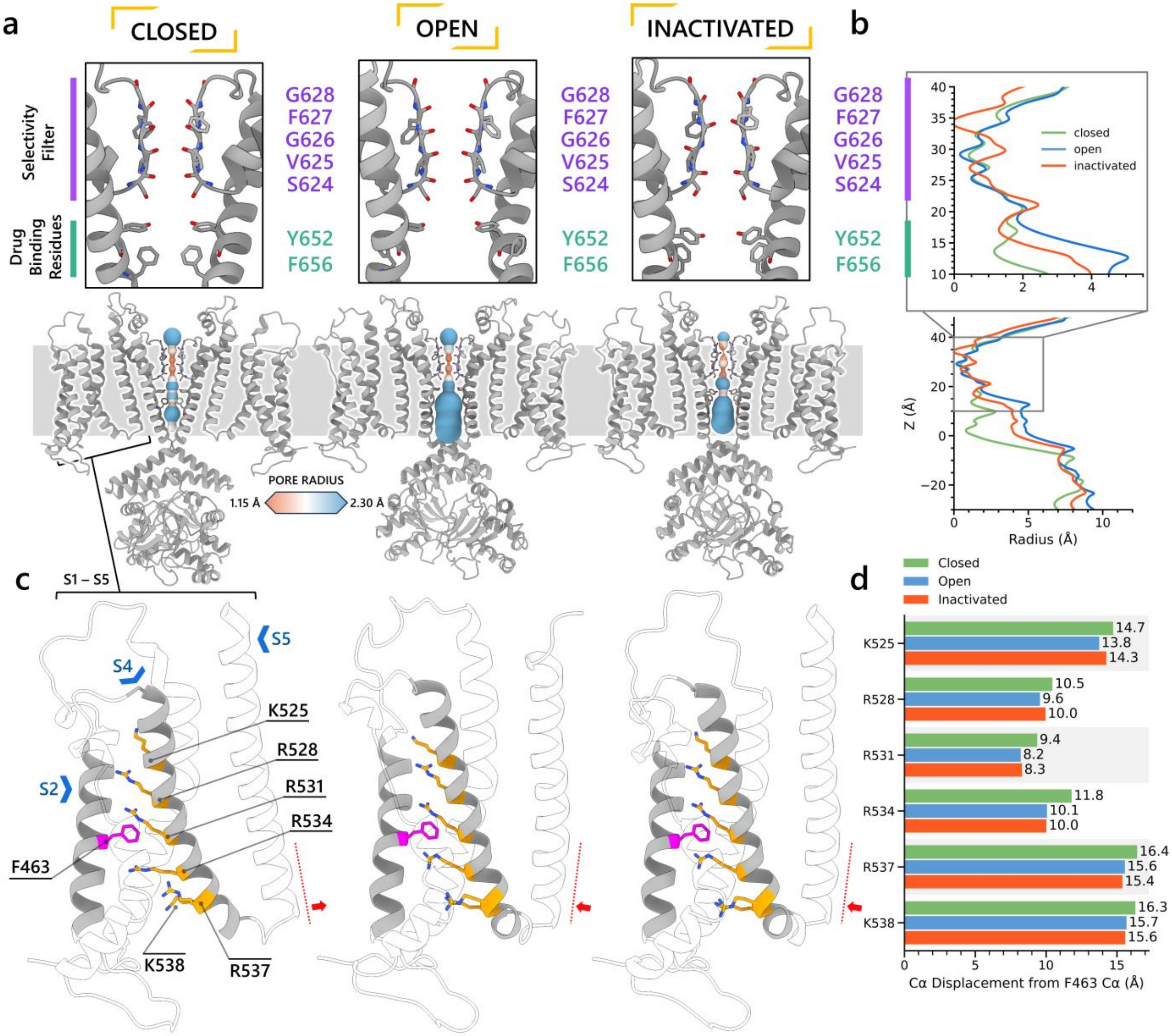

Figure 3. Structural comparison of different hERG channel state models. a) Visual comparison of the closed, open-, and inactivated-state models. **b)** Pore radius for the SF and drug binding region (upper) and for the entire pore (lower). **c)** Comparison of the VSD conformation in each model, showcasing the positively charged Arg and Lys gating-charge residues, located on the S4 helix, and the gating charge transfer center residue, F463, on the S2 helix. **d)** Measurement of the distance between the C_α atom of F463 to the C_α atom of each of the gating-charge residues.

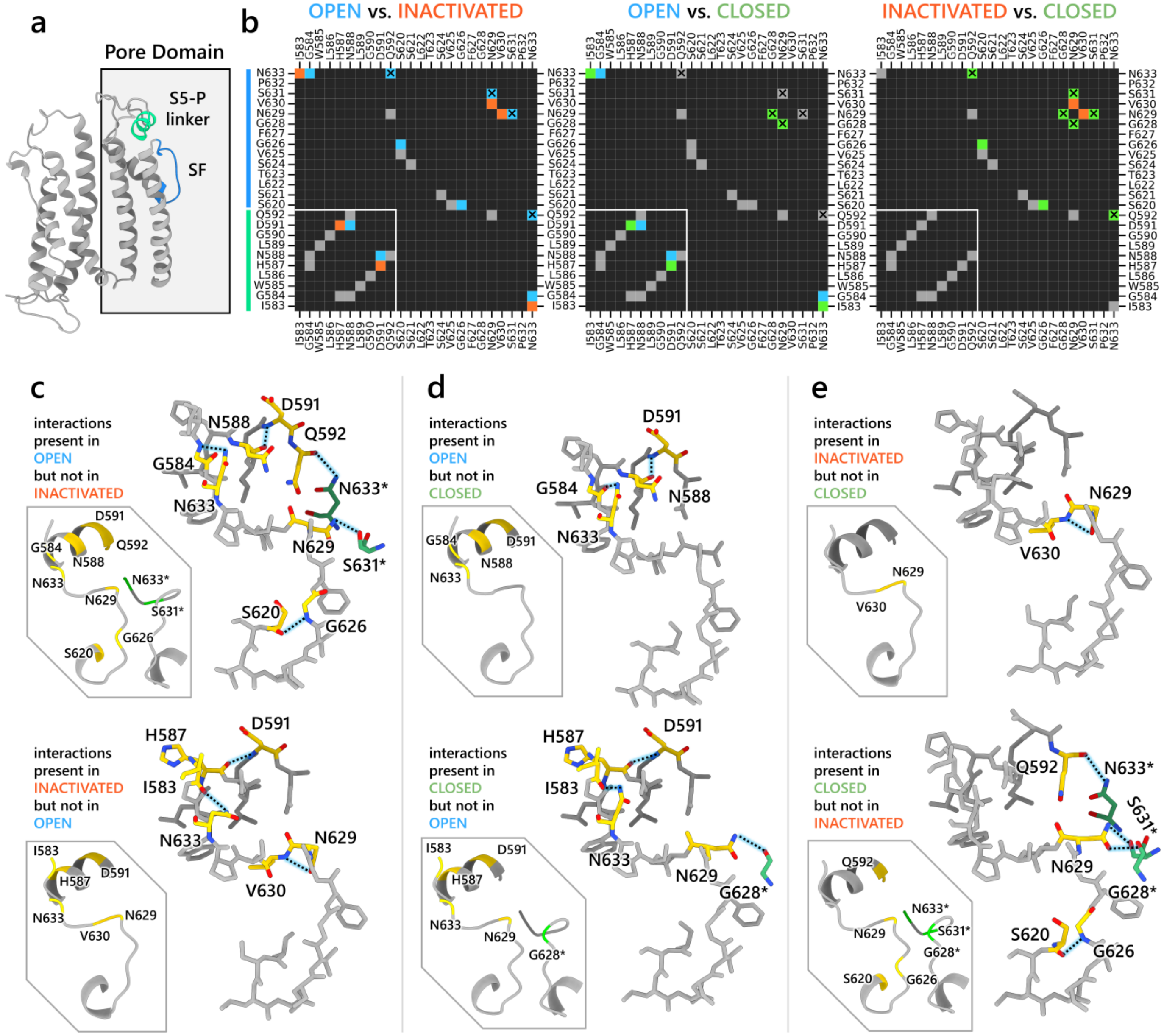
a
Pore Domain
S5-P linker
SF
b
OPEN vs. INACTIVATED
OPEN vs. CLOSED
INACTIVATED vs. CLOSED
I583 G584 W585 L586 H587 N588 L589 G590 D591 Q592 S620 S621 L622 T623 S624 V625 G626 F627 G628 N629 V630 S631 P632 N633
c
interactions present in OPEN but not in INACTIVATED
G584
N588
D591
Q592
N633
N633*
N629
S631*
S620
G626
interactions present in INACTIVATED but not in OPEN
H587
D591
I583
N633
N629
V630
d
interactions present in OPEN but not in CLOSED
D591
G584
N588
N633
interactions present in CLOSED but not in OPEN
H587
D591
I583
N633
N629
G628*
e
interactions present in INACTIVATED but not in CLOSED
N629
V630
interactions present in CLOSED but not in INACTIVATED
Q592
N633*
S631*
N629
G628*
S620
G626

Figure 4. Interaction network analysis showcasing residue-residue interactions in the S5-P linker (I583 – Q592) and region surrounding the SF (S620 – N633). a) An image of a hERG channel subunit with the analyzed regions colored in cyan and blue. **b)** Heatmaps showing intrasubunit and intersubunit (marked by X) interactions between each residue in the analyzed regions. The interactions analyzed are hydrogen bonding, π stacking, cation-π, and salt bridges. Black cells indicate no interactions. Gray cells indicate an interaction is present in both states. Blue, orange, and green colored cells indicate the interaction is present only in the open, inactivated, or closed state, respectively, but not in the other state being compared in the map. White lines are added to separate S5-P linker residues from the SF region residues. **c, d, e)** Visualization of the interactions being present in one state but not the other. Gold-colored residues are involved in the interactions. Green-colored residues, named with an asterisk at the end, are from an adjacent chain but are interacting with gold-colored residues. Dashed lines represent hydrogen bonds.

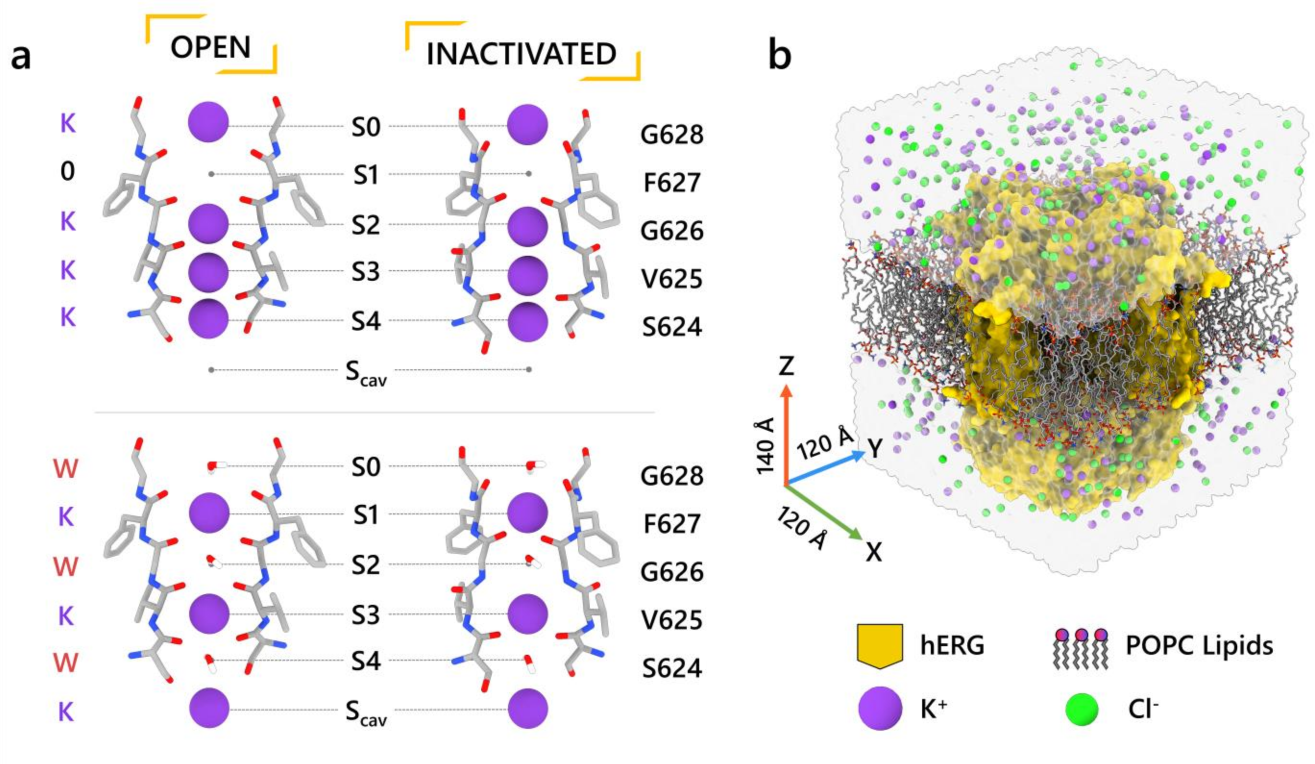
a
OPEN
INACTIVATED
K
0
K
K
K
S0
S1
S2
S3
S4
S_{cav}
G628
F627
G626
V625
S624
W
K
W
K
W
K
S0
S1
S2
S3
S4
S_{cav}
G628
F627
G626
V625
S624
b
Z
140 Å
120 Å
Y
120 Å
X
hERG
POPC Lipids
K+
Cl-

Figure 5. Setup of MD simulations to assess ion conduction in the open and inactivated models. a) Initial configuration of the SF, set to fill with either all K^+ ions, or alternating K^+ and water molecules. **b)** An example MD simulation box showing a hERG channel model (shown in yellow surface representation) embedded in POPC lipid bilayer (shown as sticks) and solvated by an aqueous 0.3 M KCl solution (shown as a transparent surface with K^+ and Cl^- ions shown as purple and green balls, respectively).

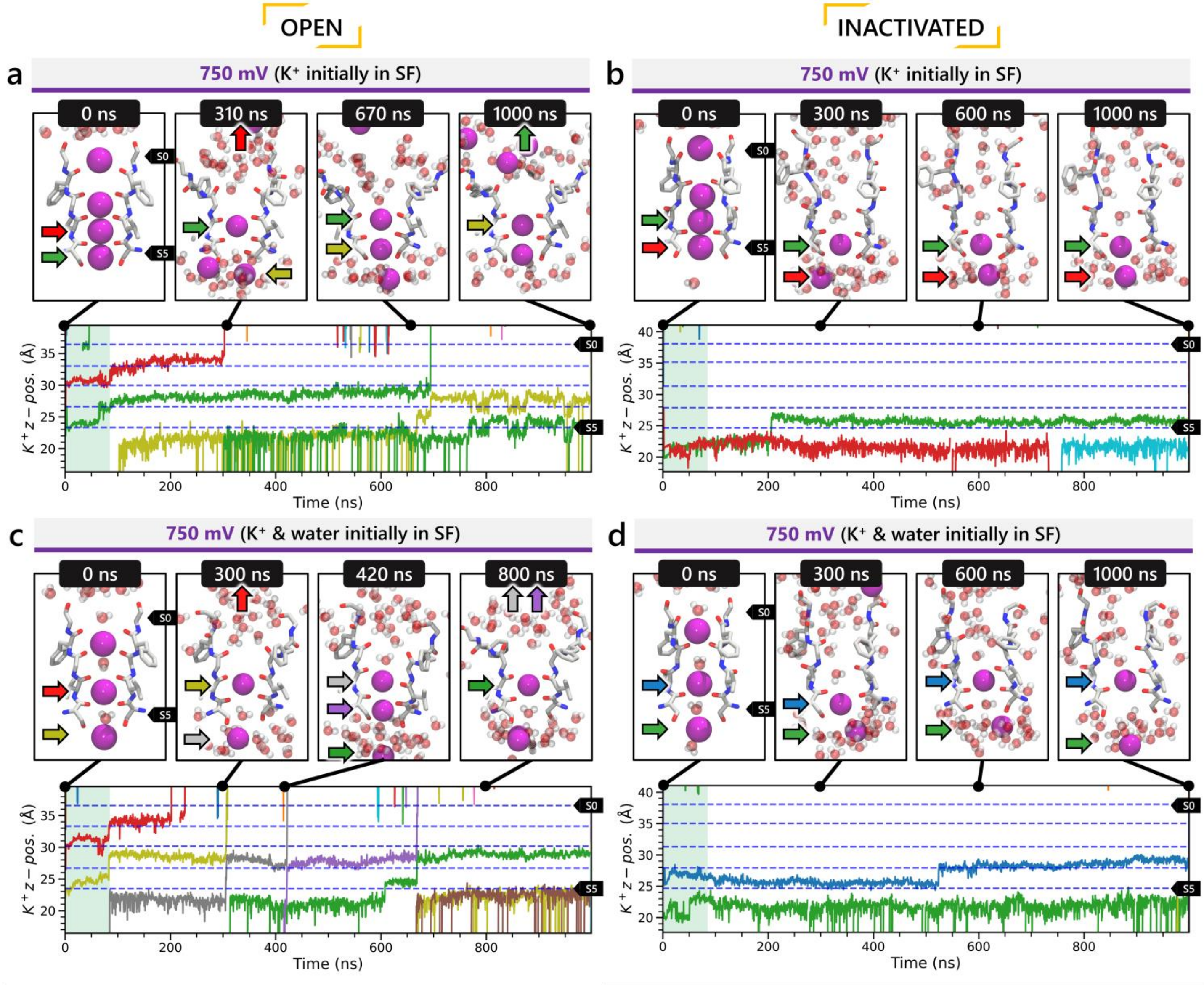

Figure 6. Movement of K⁺ ions through hERG SF. The *z* coordinates of K⁺ ions are tracked as they traverse from the pore of the channel (lower *y*-axis limit) to the extracellular space (upper *y*-axis limit) under membrane voltage of 750 mV. Putative K⁺ binding sites in the SF (S0 – S5) are marked using blue dashed lines in the plots. **a, c)** Results from MD simulations on the open model with the SF initially configured to have only K⁺ ions or alternating K⁺ / water molecules, respectively. **b, d)** Results from MD simulations on the inactivated model with the SF initially configured to have only K⁺ ions or alternating K⁺ / water molecules, respectively.

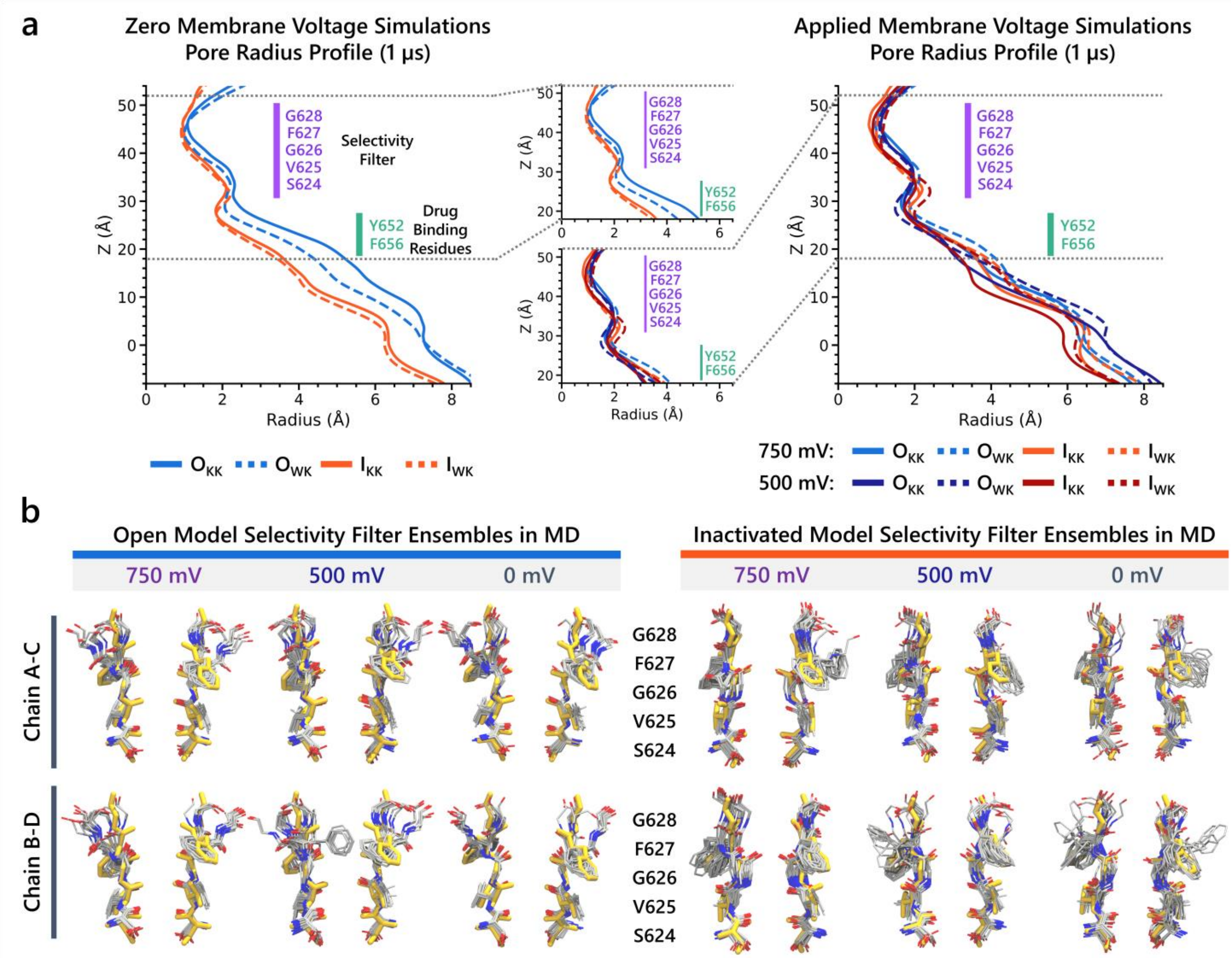

Figure 7. Analysis of dynamics of the SF and pore conformations over the course of the 1 μs MD simulations. a) Pore radius averaged over each 1 μs long MD simulations with or without applied membrane voltage. Open- and inactivated-state model MD simulations are notated as O and I, respectively, with the subscripts KK and WK denoting whether the SF initially configured to have only K^+ ions or alternating K^+ / water molecules, respectively. **b)** Ensembles of SF conformation over the course of each MD simulation superimposed over each other. The gold-colored conformation indicates the initial conformation.

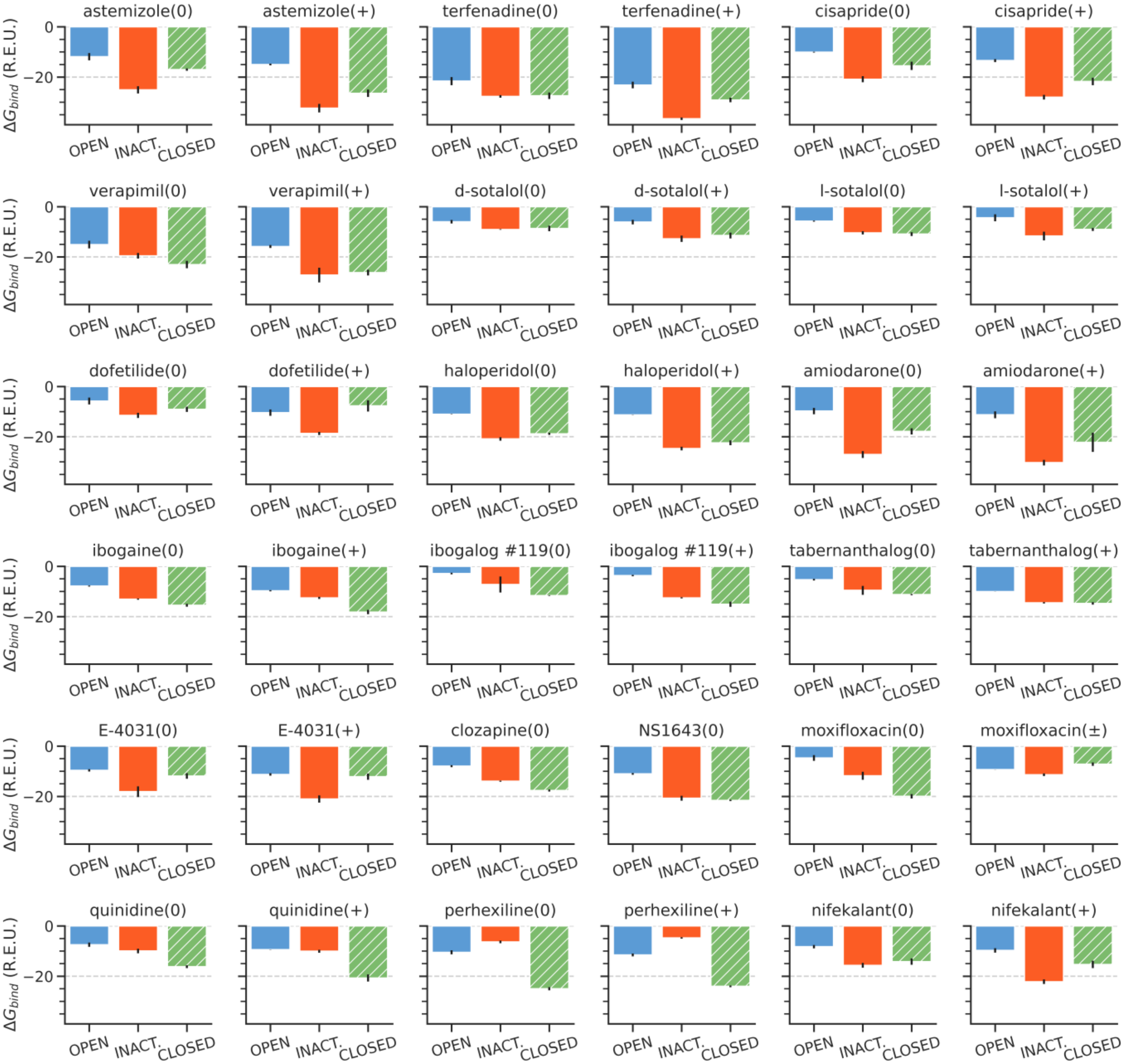

Figure 8. GALigandDock drug docking results to different hERG channel models. Each bar plot represents the estimated energy of binding in Rosetta energy units (R.E.U.) for the named drug to the open-, inactivated-, and closed-state hERG channel models. Lower values mean more favorable binding. 25,000 docking poses were generated for each drug/channel model pairing. The top 50 poses were clustered, and the plotted energy represents the average free energy of the top cluster along with the standard deviation. The labels (0), (+), (±) after the drug name indicate its neutral, cationic, or zwitterionic form, respectively.

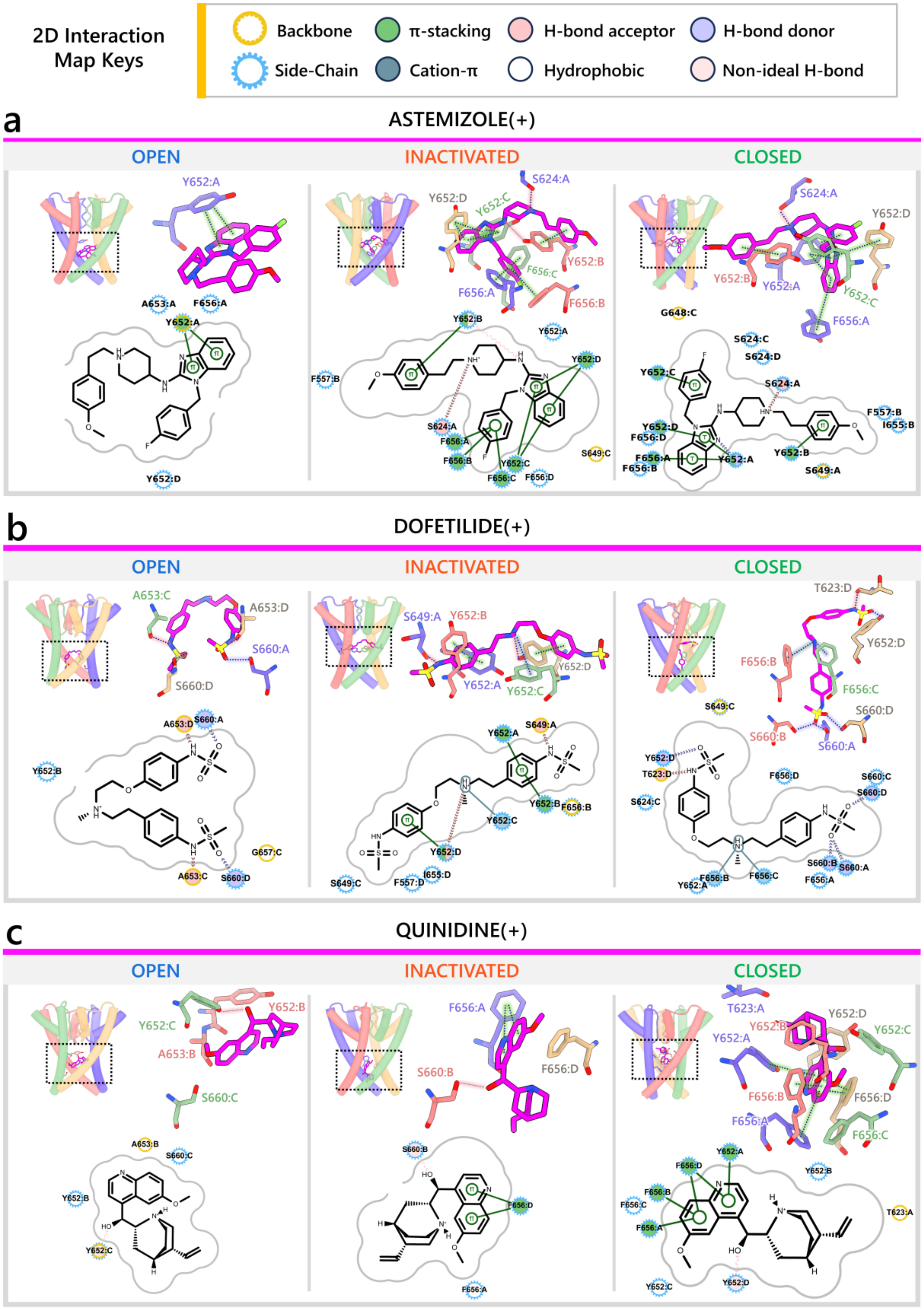
2D Interaction Map Keys
Backbone
π-stacking
H-bond acceptor
H-bond donor
Side-Chain
Cation-π
Hydrophobic
Non-ideal H-bond
a
ASTEMIZOLE(+)
OPEN
INACTIVATED
CLOSED
Y652:A
A653:A
F656:A
Y652:D
Y652:D
Y652:C
S624:A
Y652:B
F656:C
F656:A
F656:B
F557:B
S624:A
S649:C
F656:D
G648:C
S624:C
S624:D
I655:B
F557:B
Y652:C
S649:A
b
DOFETILIDE(+)
OPEN
INACTIVATED
CLOSED
A653:C
A653:D
S660:A
S660:D
Y652:B
A653:D
G657:C
A653:C
S649:A
Y652:B
Y652:A
Y652:C
Y652:D
F656:B
I655:D
F557:D
S649:C
T623:D
F656:C
S660:B
S649:C
T623:D
S624:C
F656:D
S660:C
F656:A
c
QUINIDINE(+)
OPEN
INACTIVATED
CLOSED
Y652:C
Y652:B
A653:B
S660:C
A653:B
S660:C
Y652:B
Y652:C
F656:A
S660:B
F656:D
F656:A
T623:A
Y652:B
Y652:D
Y652:C
Y652:A
F656:B
F656:D
F656:C
F656:A
T623:A
Y652:D
Y652:C

Figure 9. Visualization of interactions for cationic astemizole (a), dofetilide (b), and quinidine (c) to different hERG channel models. Each panel includes 3 subpanels showcasing drug interactions to the open-, inactivated, and closed-state hERG channel models. In each subpanel, an overview of where the drug binds within the channel pore is shown on the upper left, a 3D visualization of interactions between each channel residue (blue, red, green, and tan residues are from the subunit A, B, C, or D, respectively) to the drug (magenta) is shown on the upper right, and a 2D ligand – protein interaction map is shown at the bottom. A continuous gray line depicts the contour of the protein binding site, and any breaks in this line signal areas where the ligand is exposed to the solvent.

References

1. J. I. Vandenberg, *et al.*, hERG K(+) channels: structure, function, and clinical significance. *Physiol. Rev.* **92**, 1393–1478 (2012).

2. M. C. Sanguinetti, M. Tristani-Firouzi, hERG potassium channels and cardiac arrhythmia. *Nature* **440**, 463–469 (2006).

3. M. Li, L. G. Ramos, Drug-Induced QT Prolongation And Torsades de Pointes. *Pharm. Ther.* **42**, 473–477 (2017).

4. N. Ferri, *et al.*, Drug attrition during pre-clinical and clinical development: understanding and managing drug-induced cardiotoxicity. *Pharmacol. Ther.* **138**, 470–484 (2013).

5. K. Kocadal, S. Saygi, F. B. Alkas, S. Sardas, Drug-associated cardiovascular risks: A retrospective evaluation of withdrawn drugs. *North. Clin. Istanb.* **6**, 196–202 (2018).

6. A. L. Waldo, *et al.*, Effect of d-sotalol on mortality in patients with left ventricular dysfunction after recent and remote myocardial infarction. *The Lancet* **348**, 7–12 (1996).

7. W. Wang, R. MacKinnon, Cryo-EM Structure of the Open Human Ether-à-go-go-Related K+ Channel hERG. *Cell* **169**, 422-430.e10 (2017).

8. M. J. Perrin, P. W. Kuchel, T. J. Campbell, J. I. Vandenberg, Drug Binding to the Inactivated State Is Necessary but Not Sufficient for High-Affinity Binding to Human Ether-à-go-go-Related Gene Channels. *Mol. Pharmacol.* **74**, 1443–1452 (2008).

9. B. Priest, I. M. Bell, M. Garcia, Role of hERG potassium channel assays in drug development. *Channels* **2**, 87–93 (2008).

10. T. Asai, *et al.*, Cryo-EM Structure of K+-Bound hERG Channel Complexed with the Blocker Astemizole. *Struct. Lond. Engl. 1993* **29**, 203-212.e4 (2021).

11. P.-C. Yang, *et al.*, A Computational Pipeline to Predict Cardiotoxicity: From the Atom to the Rhythm. *Circ. Res.* **126**, 947–964 (2020).

12. J. Jumper, *et al.*, Highly accurate protein structure prediction with AlphaFold. *Nature* **596**, 583–589 (2021).

13. H. Park, G. Zhou, M. Baek, D. Baker, F. DiMaio, Force Field Optimization Guided by Small Molecule Crystal Lattice Data Enables Consistent Sub-Angstrom Protein-Ligand Docking. *J. Chem. Theory Comput.* **17**, 2000–2010 (2021).

14. W. E. Miranda, *et al.*, Selectivity filter modalities and rapid inactivation of the hERG1 channel. *Proc. Natl. Acad. Sci.* **117**, 2795–2804 (2020).

15. J. Li, R. Shen, B. Reddy, E. Perozo, B. Roux, Mechanism of C-type inactivation in the hERG potassium channel. *Sci. Adv.* **7**, eabd6203 (2021).

16. D. Sala, P. W. Hildebrand, J. Meiler, Biasing AlphaFold2 to predict GPCRs and kinases with user-defined functional or structural properties. *Front. Mol. Biosci.* **10**, 1121962 (2023).

17. D. del Alamo, D. Sala, H. S. Mchaourab, J. Meiler, Sampling alternative conformational states of transporters and receptors with AlphaFold2. *eLife* **11**, e75751 (2022).

18. B. P. Brown, R. A. Stein, J. Meiler, H. S. Mchaourab, Approximating Projections of Conformational Boltzmann Distributions with AlphaFold2 Predictions: Opportunities and Limitations. *J. Chem. Theory Comput.* (2024) https:/doi.org/10.1021/acs.jctc.3c01081 (January 25, 2024).

19. J. Maly, *et al.*, Structural modeling of the hERG potassium channel and associated drug interactions. *Front. Pharmacol.* **13**, 966463 (2022).

20. A. M. Emigh Cortez, *et al.*, Structural modeling of hERG channel-drug interactions using Rosetta. *Front. Pharmacol.* **14**, 1244166 (2023).

21. V. S. Mandala, R. MacKinnon, Voltage-sensor movements in the Eag Kv channel under an applied electric field. *Proc. Natl. Acad. Sci. U. S. A.* **119**, e2214151119 (2022).

22. M. Mirdita, *et al.*, ColabFold: making protein folding accessible to all. *Nat. Methods* **19**, 679–682 (2022).

23. M. Mirdita, M. Steinegger, J. Söding, MMseqs2 desktop and local web server app for fast, interactive sequence searches. *Bioinforma. Oxf. Engl.* **35**, 2856–2858 (2019).

24. P. Phartiyal, E. M. C. Jones, G. A. Robertson, Heteromeric Assembly of Human Ether-à-go-go-related Gene (hERG) 1a/1b Channels Occurs Cotranslationally via N-terminal Interactions*. *J. Biol. Chem.* **282**, 9874–9882 (2007).

25. S. J. Fleishman, *et al.*, RosettaScripts: A Scripting Language Interface to the Rosetta Macromolecular Modeling Suite. *PLOS ONE* **6**, e20161 (2011).

26. Carus H.Y. Lau, *et al.*, Potassium dependent structural changes in the selectivity filter of HERG potassium channels. *bioRxiv*, 2023.12.14.571769 (2023).

27. J. Vandenberg, *et al.*, Structural Basis for Rapid Voltage Dependent Inactivation of HERG Potassium Channels. *ResearchSquare* (2021) https:/doi.org/10.21203/rs.3.rs-1105661/v1.

28. J. K. Leman, *et al.*, Macromolecular modeling and design in Rosetta: recent methods and frameworks. *Nat. Methods* **17**, 665–680 (2020).

29. D. A. Doyle, *et al.*, The structure of the potassium channel: molecular basis of K+ conduction and selectivity. *Science* **280**, 69–77 (1998).

30. S. B. Long, E. B. Campbell, R. Mackinnon, Crystal structure of a mammalian voltage-dependent Shaker family K+ channel. *Science* **309**, 897–903 (2005).

31. L. G. Cuello, V. Jogini, D. M. Cortes, E. Perozo, Structural mechanism of C-type inactivation in K+ channels. *Nature* **466**, 203–208 (2010).

32. X.-F. Tan, *et al.*, Structure of the Shaker Kv channel and mechanism of slow C-type inactivation. *Sci. Adv.* **8**, eabm7814.

33. A. Tyagi, *et al.*, Rearrangement of a unique Kv1.3 selectivity filter conformation upon binding of a drug. *Proc. Natl. Acad. Sci. U. S. A.* **119**, e2113536119 (2022).

34. K. G. Chandy, K. Sanches, R. S. Norton, Structure of the voltage-gated potassium channel KV1.3: Insights into the inactivated conformation and binding to therapeutic leads. *Channels* **17**, 2253104.

35. P. Selvakumar, *et al.*, Structures of the T cell potassium channel Kv1.3 with immunoglobulin modulators. *Nat. Commun.* **13**, 3854 (2022).

36. J. K. Noel, P. C. Whitford, J. N. Onuchic, The Shadow Map: A General Contact Definition for Capturing the Dynamics of Biomolecular Folding and Function. *J. Phys. Chem. B* **116**, 8692–8702 (2012).

37. W. Dun, M. Jiang, G.-N. Tseng, Allosteric effects of mutations in the extracellular S5-P loop on the gating and ion permeation properties of the hERG potassium channel. *Pflüg. Arch.* **439**, 141–149 (1999).

38. A. Butler, Y. Zhang, A. G. Stuart, C. E. Dempsey, J. C. Hancox, Action potential clamp characterization of the S631A hERG mutation associated with short QT syndrome. *Physiol. Rep.* **6**, e13845 (2018).

39. J. S. Fan, M. Jiang, W. Dun, T. V. McDonald, G. N. Tseng, Effects of outer mouth mutations on hERG channel function: a comparison with similar mutations in the Shaker channel. *Biophys. J.* **76**, 3128–3140 (1999).

40. C. A. Satler, M. R. Vesely, P. Duggal, G. S. Ginsburg, A. H. Beggs, Multiple different missense mutations in the pore region of HERG in patients with long QT syndrome. *Hum. Genet.* **102**, 265–272 (1998).

41. J. M. Cordeiro, R. Brugada, Y. S. Wu, K. Hong, R. Dumaine, Modulation of IKr inactivation by mutation N588K in KCNH2: A link to arrhythmogenesis in short QT syndrome. *Cardiovasc. Res.* **67**, 498–509 (2005).

42. C. E. Clarke, *et al.*, Effect of S5P α-helix charge mutants on inactivation of hERG K+ channels. *J. Physiol.* **573**, 291–304 (2006).

43. E. Ficker, W. Jarolimek, J. Kiehn, A. Baumann, A. M. Brown, Molecular determinants of dofetilide block of HERG K+ channels. *Circ. Res.* **82**, 386–395 (1998).

44. T. Nakajima, *et al.*, Novel Mechanism of HERG Current Suppression in LQT2. *Circ. Res.* **83**, 415–422 (1998).

45. J. T. Zhao, *et al.*, Not all hERG pore domain mutations have a severe phenotype: G584S has an inactivation gating defect with mild phenotype compared to G572S, which has a dominant negative trafficking defect and a severe phenotype. *J. Cardiovasc. Electrophysiol.* **20**, 923–930 (2009).

46. J. Liu, M. Zhang, M. Jiang, G.-N. Tseng, Structural and Functional Role of the Extracellular S5-P Linker in the HERG Potassium Channel. *J. Gen. Physiol.* **120**, 723–737 (2002).

47. S. Thouta, *et al.*, Proline Scan of the hERG Channel S6 Helix Reveals the Location of the Intracellular Pore Gate. *Biophys. J.* **106**, 1057–1069 (2014).

48. M. V. Helliwell, *et al.*, Structural implications of hERG K+ channel block by a high-affinity minimally structured blocker. *J. Biol. Chem.* **293**, 7040–7057 (2018).

49. C. K. Lam, B. L. de Groot, Ion Conduction Mechanisms in Potassium Channels Revealed by Permeation Cycles. *J. Chem. Theory Comput.* **19**, 2574–2589 (2023).

50. B. Roux, Ion channels and ion selectivity. *Essays Biochem.* **61**, 201–209 (2017).

51. H. Numaguchi, *et al.*, Probing the Interaction Between Inactivation Gating and dd-Sotalol Block of HERG. *Circ. Res.* **87**, 1012–1018 (2000).

52. S. Wang, M. J. Morales, S. Liu, H. C. Strauss, R. L. Rasmusson, Modulation of HERG affinity for E-4031 by [K+]o and C-type inactivation. *FEBS Lett.* **417**, 43–47 (1997).

53. A. J. Alexandrou, *et al.*, Mechanism of hERG K+ channel blockade by the fluoroquinolone antibiotic moxifloxacin. *Br. J. Pharmacol.* **147**, 905–916 (2006).

54. M. J. Windley, *et al.*, Measuring kinetics and potency of hERG block for CiPA. *J. Pharmacol. Toxicol. Methods* **87**, 99–107 (2017).

55. A. Windisch, *et al.*, Trapping and dissociation of propafenone derivatives in HERG channels. *Br. J. Pharmacol.* **162**, 1542 (2011).

56. K. Kamiya, R. Niwa, J. S. Mitcheson, M. C. Sanguinetti, Molecular Determinants of hERG Channel Block. *Mol. Pharmacol.* **69**, 1709–1716 (2006).

57. D. Stork, *et al.*, State dependent dissociation of HERG channel inhibitors. *Br. J. Pharmacol.* **151**, 1368–1376 (2007).

58. Y. Miao, A. Bhattarai, J. Wang, Ligand Gaussian accelerated molecular dynamics (LiGaMD): Characterization of ligand binding thermodynamics and kinetics. *J. Chem. Theory Comput.* **16**, 5526–5547 (2020).

59. D. Branduardi, J. D. Faraldo-Gómez, String method for calculation of minimum free-energy paths in Cartesian space in freely-tumbling systems. *J. Chem. Theory Comput.* **9**, 4140–4154 (2013).

60. , OEPerceiveInteractionOptions — Toolkits -- Python (January 16, 2024).

61. P. Saxena, *et al.*, New potential binding determinant for hERG channel inhibitors. *Sci. Rep.* **6**, 24182 (2016).

62. , Solving the hERG anti-target with cryo-EM | Nano Imaging (January 9, 2024).

63. S. Z. Stepanovic, *et al.*, The evolutionarily conserved residue A653 plays a key role in HERG channel closing. *J. Physiol.* **587**, 2555–2566 (2009).

64. Y. Wang, *et al.*, Role of the pH in state-dependent blockade of hERG currents. *Sci. Rep.* **6**, 32536 (2016).

65. J. A. Sănchez-Chapula, T. Ferrer, R. A. Navarro-Polanco, M. C. Sanguinetti, Voltage-dependent profile of human ether-a-go-go-related gene channel block is influenced by a single residue in the S6 transmembrane domain. *Mol. Pharmacol.* **63**, 1051–1058 (2003).

66. M. AlQuraishi, AlphaFold at CASP13. *Bioinforma. Oxf. Engl.* **35**, 4862–4865 (2019).

67. J. Jumper, *et al.*, Applying and improving AlphaFold at CASP14. *Proteins* **89**, 1711–1721 (2021).

68. M. Varadi, S. Velankar, The impact of AlphaFold Protein Structure Database on the fields of life sciences. *Proteomics* **23**, e2200128 (2023).

69. M. Karelina, J. J. Noh, R. O. Dror, How accurately can one predict drug binding modes using AlphaFold models? *eLife* **12**, RP89386 (2023).

70. K. R. DeMarco, *et al.*, Molecular determinants of pro-arrhythmia proclivity of d- and l-sotalol via a multi-scale modeling pipeline. *J. Mol. Cell. Cardiol.* **158**, 163–177 (2021).

71. M. Baek, *et al.*, Accurate prediction of protein structures and interactions using a three-track neural network. *Science* **373**, 871–876 (2021).

72. H. M. Berman, *et al.*, The Protein Data Bank. *Nucleic Acids Res.* **28**, 235–242 (2000).

73. S. Jo, T. Kim, V. G. Iyer, W. Im, CHARMM-GUI: A web-based graphical user interface for CHARMM. *J. Comput. Chem.* **29**, 1859–1865 (2008).

74. D. A. Case, *et al.*, The Amber biomolecular simulation programs. *J. Comput. Chem.* **26**, 1668–1688 (2005).

75. J. Huang, A. D. MacKerell Jr, CHARMM36 all-atom additive protein force field: Validation based on comparison to NMR data. *J. Comput. Chem.* **34**, 2135–2145 (2013).

76. J. B. Klauda, *et al.*, Update of the CHARMM All-Atom Additive Force Field for Lipids: Validation on Six Lipid Types. *J. Phys. Chem. B* **114**, 7830–7843 (2010).

77. W. L. Jorgensen, J. Chandrasekhar, J. D. Madura, R. W. Impey, M. L. Klein, Comparison of simple potential functions for simulating liquid water. *J. Chem. Phys.* **79**, 926–935 (1983).

78. T. Darden, D. York, L. Pedersen, Particle mesh Ewald: An N·log(N) method for Ewald sums in large systems. *J. Chem. Phys.* **98**, 10089–10092 (1993).

79. S. Kim, *et al.*, PubChem Substance and Compound databases. *Nucleic Acids Res.* **44**, D1202-1213 (2016).

80. B. I. Tingle, *et al.*, ZINC-22–A Free Multi-Billion-Scale Database of Tangible Compounds for Ligand Discovery. *J. Chem. Inf. Model.* **63**, 1166–1176 (2023).

81. M. D. Hanwell, *et al.*, Avogadro: an advanced semantic chemical editor, visualization, and analysis platform. *J. Cheminformatics* **4**, 17 (2012).

82. D. A. Case, *et al.*, AmberTools. *J. Chem. Inf. Model.* **63**, 6183–6191 (2023).

83. , Molecular Modeling Software | OpenEye Scientific (January 1, 2024).

84. E. F. Pettersen, *et al.*, UCSF ChimeraX: Structure visualization for researchers, educators, and developers. *Protein Sci. Publ. Protein Soc.* **30**, 70–82 (2021).

85. W. Humphrey, A. Dalke, K. Schulten, VMD: visual molecular dynamics. *J. Mol. Graph.* **14**, 33–38, 27–28 (1996).

86. S. Salentin, S. Schreiber, V. J. Haupt, M. F. Adasme, M. Schroeder, PLIP: fully automated protein–ligand interaction profiler. *Nucleic Acids Res.* **43**, W443–W447 (2015).

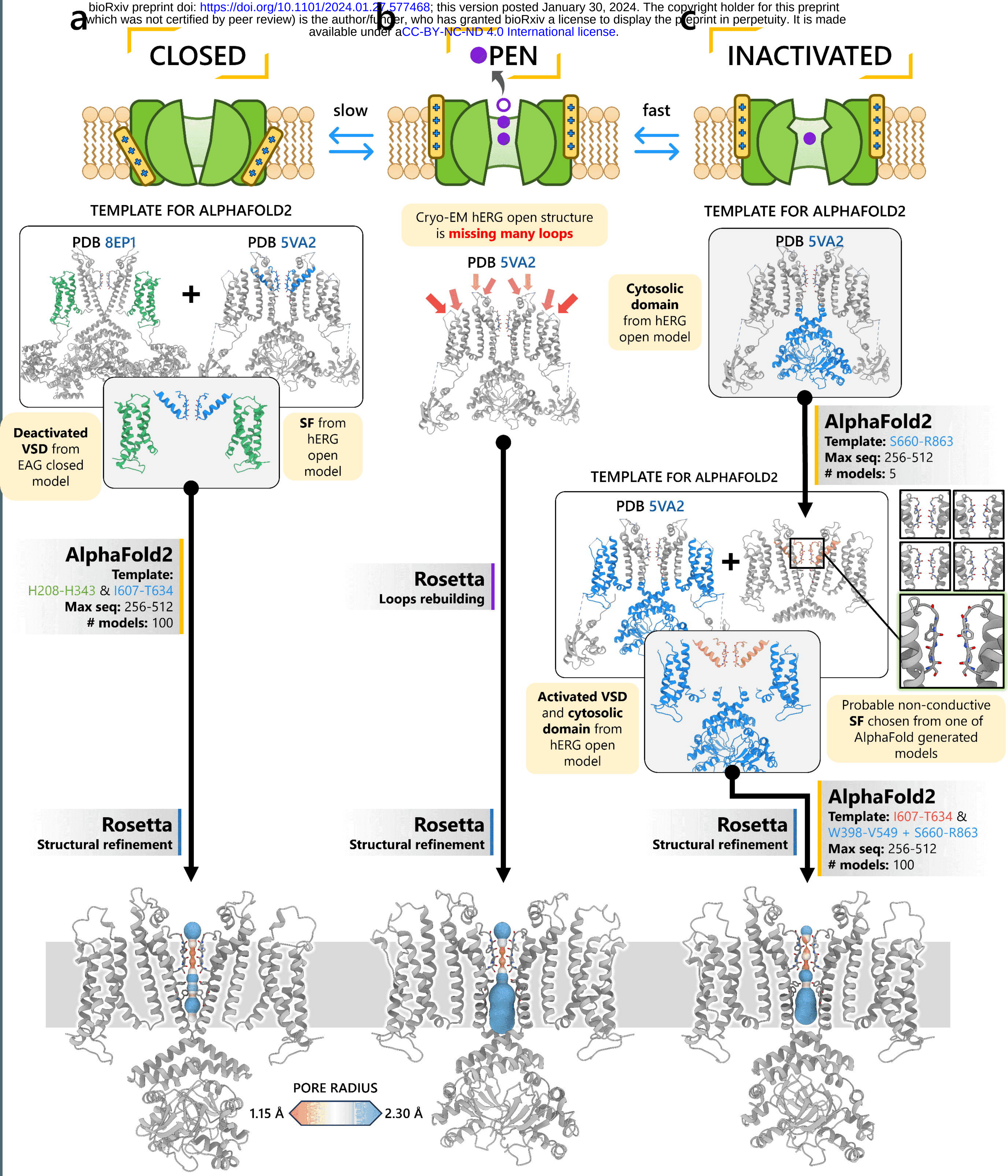
a
b
c
CLOSED
OPEN
INACTIVATED
slow
fast
TEMPLATE FOR ALPHAFOLD2
PDB 8EP1
+
PDB 5VA2
Deactivated VSD from EAG closed model
SF from hERG open model
AlphaFold2
Template:
H208-H343 & I607-T634
Max seq: 256-512
# models: 100
Rosetta
Structural refinement
Cryo-EM hERG open structure is missing many loops
PDB 5VA2
Rosetta
Loops rebuilding
Rosetta
Structural refinement
TEMPLATE FOR ALPHAFOLD2
PDB 5VA2
Cytosolic domain from hERG open model
AlphaFold2
Template: S660-R863
Max seq: 256-512
# models: 5
TEMPLATE FOR ALPHAFOLD2
PDB 5VA2
+
Activated VSD and cytosolic domain from hERG open model
Probable non-conductive SF chosen from one of AlphaFold generated models
AlphaFold2
Template: I607-T634 &
W398-V549 + S660-R863
Max seq: 256-512
# models: 100
Rosetta
Structural refinement
PORE RADIUS
1.15 Å
2.30 Å

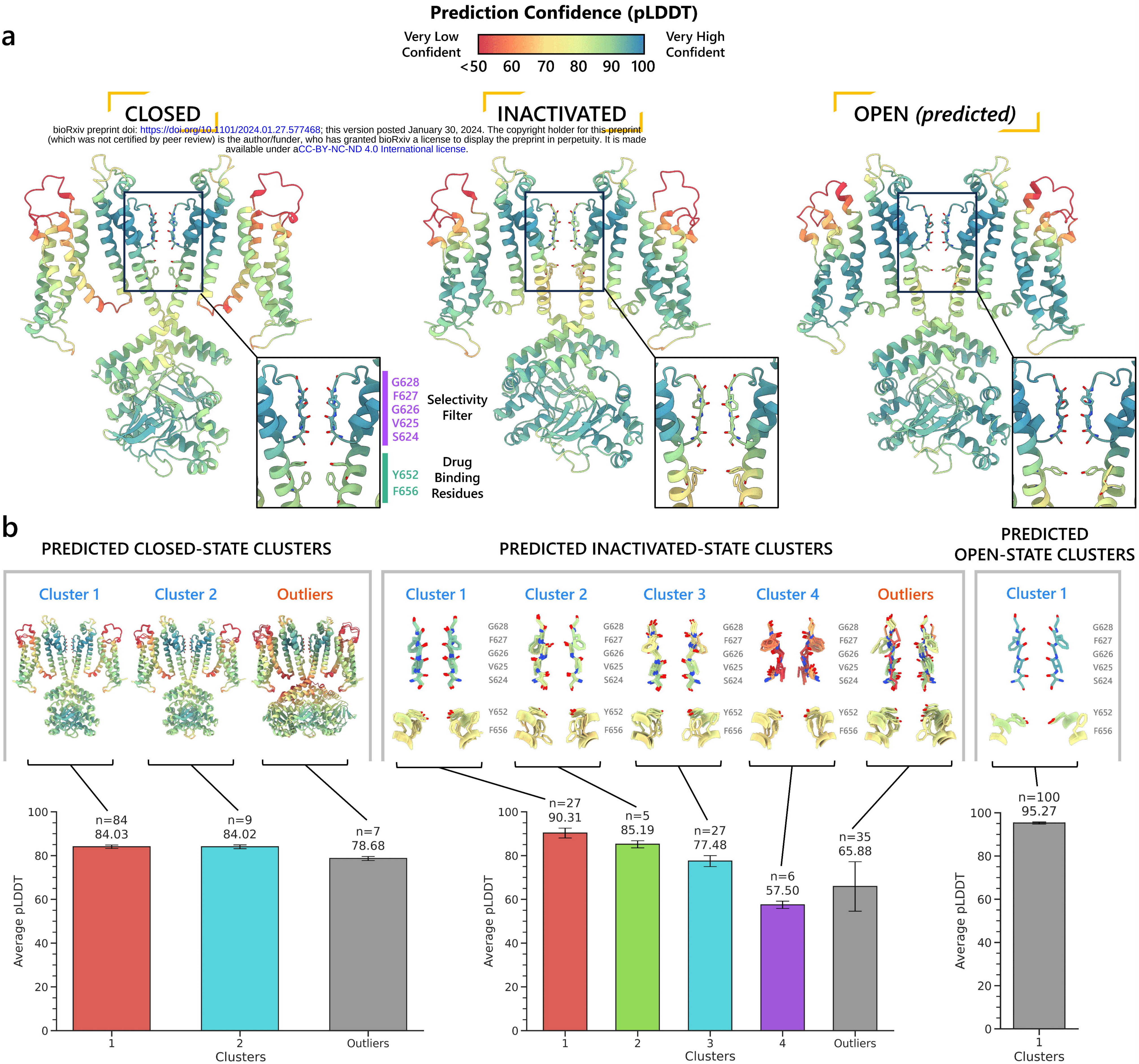
a
Prediction Confidence (pLDDT)
Very Low Confident
Very High Confident
<50
60
70
80
90
100
CLOSED
INACTIVATED
OPEN (predicted)
G628
F627
G626
V625
S624
Selectivity Filter
Y652
F656
Drug Binding Residues
b
PREDICTED CLOSED-STATE CLUSTERS
PREDICTED INACTIVATED-STATE CLUSTERS
PREDICTED OPEN-STATE CLUSTERS
Cluster 1
Cluster 2
Outliers
Cluster 1
Cluster 2
Cluster 3
Cluster 4
Outliers
Cluster 1
G628
F627
G626
V625
S624
Y652
F656
n=84
84.03
n=9
84.02
n=7
78.68
n=27
90.31
n=5
85.19
n=27
77.48
n=6
57.50
n=35
65.88
n=100
95.27
Average pLDDT
0
20
40
60
80
100
1
2
Outliers
1
2
3
4
Outliers
1
Clusters

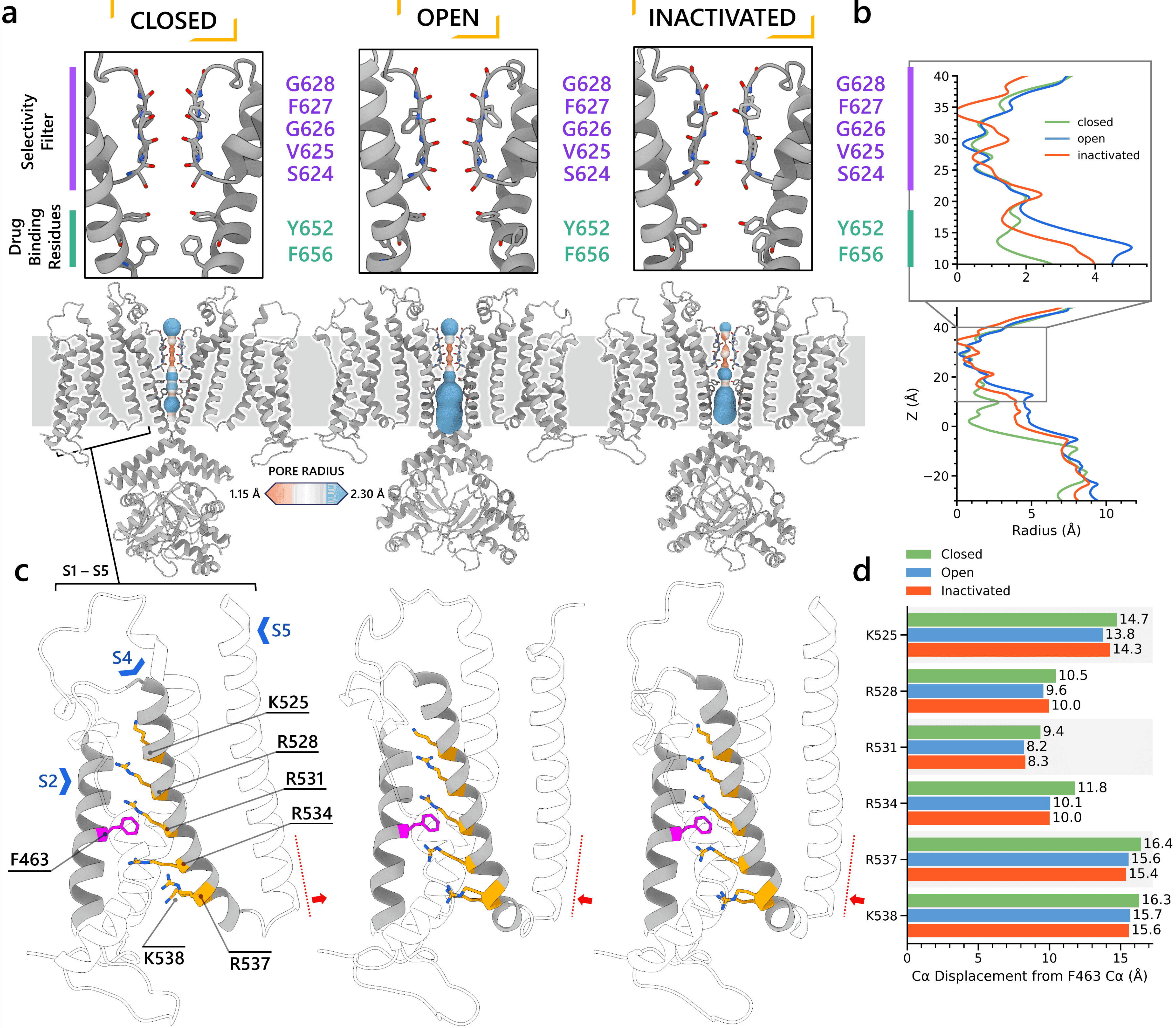
a
CLOSED
OPEN
INACTIVATED
Selectivity Filter
Drug Binding Residues
G628
F627
G626
V625
S624
Y652
F656
PORE RADIUS
1.15 Å
2.30 Å
b
closed
open
inactivated
Z (Å)
Radius (Å)
40
35
30
25
20
15
10
0
2
4
20
0
−20
5
10
c
S1 – S5
S5
S4
S2
K525
R528
R531
R534
F463
K538
R537
d
Closed
Open
Inactivated
K525
14.7
13.8
14.3
R528
10.5
9.6
10.0
R531
9.4
8.2
8.3
R534
11.8
10.1
10.0
R537
16.4
15.6
15.4
K538
16.3
15.7
15.6
0
5
10
15
Cα Displacement from F463 Cα (Å)

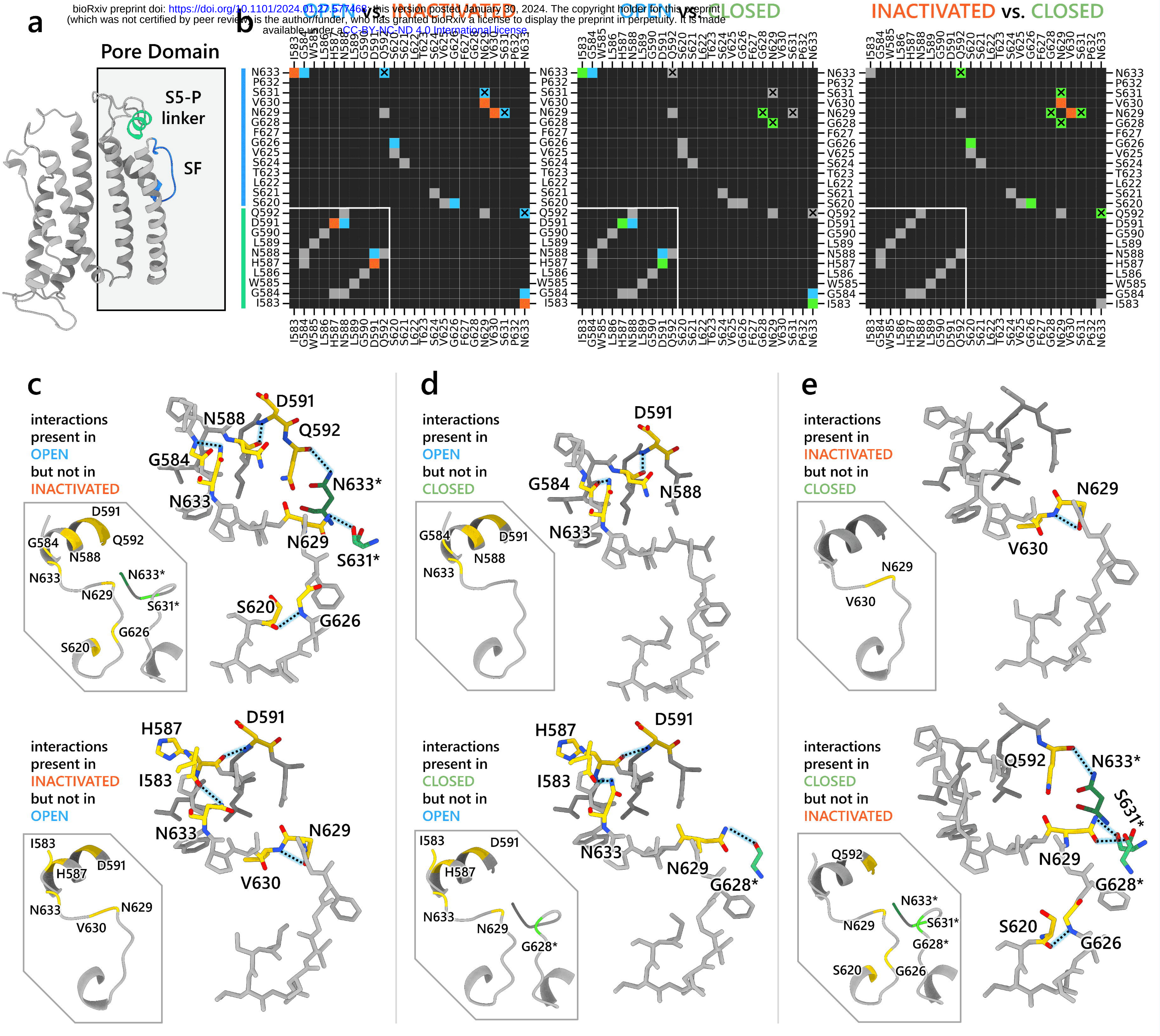
a
Pore Domain
S5-P linker
SF
b
OPEN vs. INACTIVATED
OPEN vs. CLOSED
INACTIVATED vs. CLOSED
I583
G584
W585
L586
H587
N588
L589
G590
D591
Q592
S620
S621
L622
T623
S624
V625
G626
F627
G628
N629
V630
S631
P632
N633
c
interactions present in OPEN but not in INACTIVATED
D591
N588
Q592
G584
N633*
N633
N629
S631*
S620
G626
interactions present in INACTIVATED but not in OPEN
H587
D591
I583
N633
N629
V630
d
interactions present in OPEN but not in CLOSED
D591
G584
N588
N633
interactions present in CLOSED but not in OPEN
H587
D591
I583
N633
N629
G628*
e
interactions present in INACTIVATED but not in CLOSED
N629
V630
interactions present in CLOSED but not in INACTIVATED
Q592
N633*
S631*
N629
G628*
S620
G626

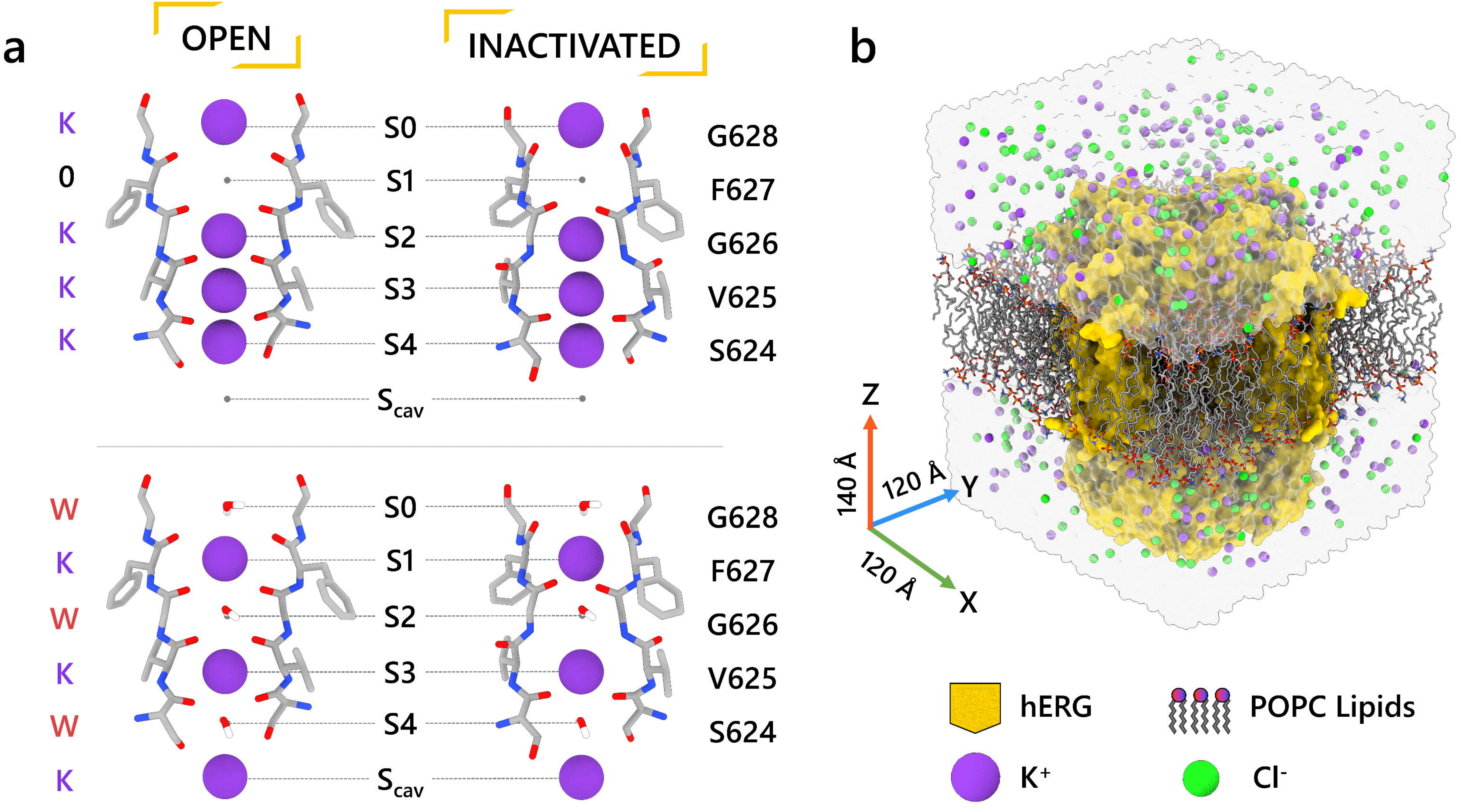
a
OPEN
INACTIVATED
K
0
K
K
K
S0
S1
S2
S3
S4
S$_{cav}$
G628
F627
G626
V625
S624
W
K
W
K
W
K
S0
S1
S2
S3
S4
S$_{cav}$
G628
F627
G626
V625
S624
b
Z
140 Å
120 Å
Y
120 Å
X
hERG
POPC Lipids
K$^+$
Cl$^-$

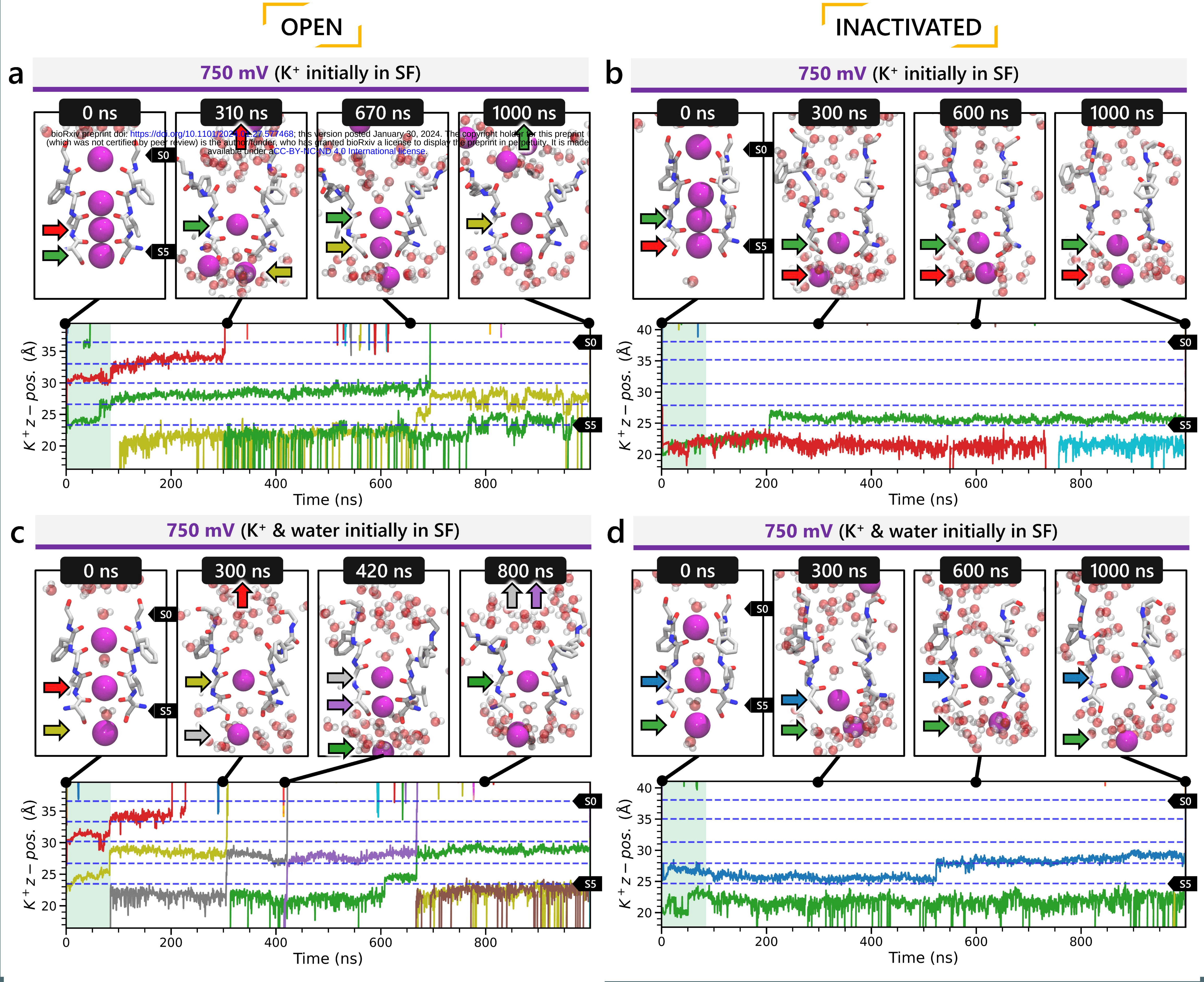
OPEN
INACTIVATED
a
750 mV (K⁺ initially in SF)
0 ns
310 ns
670 ns
1000 ns
S0
S5
K^+ z − pos. (Å)
Time (ns)
b
750 mV (K⁺ initially in SF)
0 ns
300 ns
600 ns
1000 ns
c
750 mV (K⁺ & water initially in SF)
0 ns
300 ns
420 ns
800 ns
d
750 mV (K⁺ & water initially in SF)
0 ns
300 ns
600 ns
1000 ns
20
25
30
35
40
0
200
400
600
800

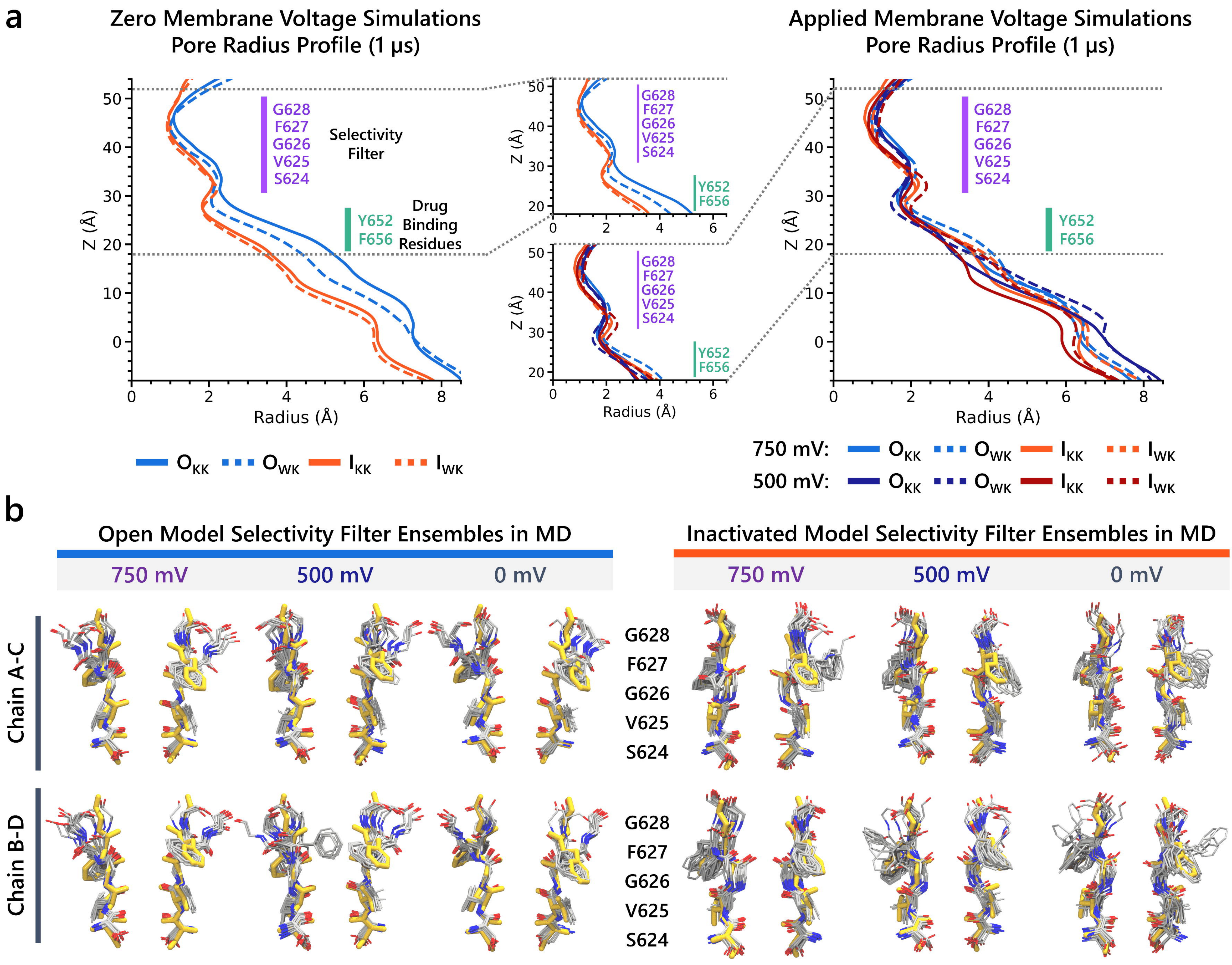
a
Zero Membrane Voltage Simulations
Pore Radius Profile (1 μs)
Applied Membrane Voltage Simulations
Pore Radius Profile (1 μs)
G628
F627
G626
V625
S624
Selectivity Filter
Y652
F656
Drug Binding Residues
Z (Å)
Radius (Å)
0
2
4
6
8
50
40
30
20
10
0
O_{KK}
O_{WK}
I_{KK}
I_{WK}
750 mV:
500 mV:
b
Open Model Selectivity Filter Ensembles in MD
Inactivated Model Selectivity Filter Ensembles in MD
750 mV
500 mV
0 mV
Chain A-C
Chain B-D
G628
F627
G626
V625
S624

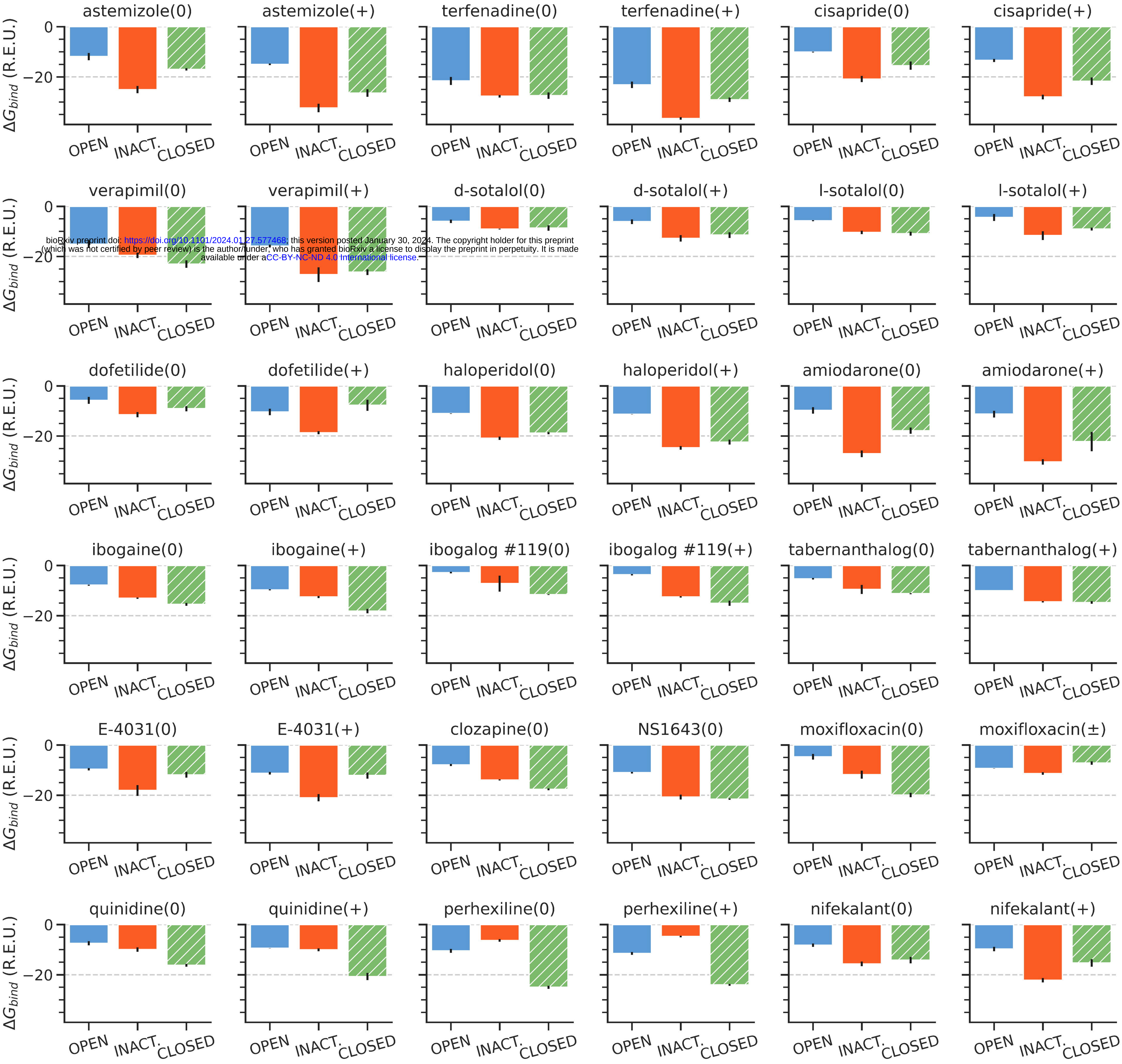
astemizole(0)
astemizole(+)
terfenadine(0)
terfenadine(+)
cisapride(0)
cisapride(+)
verapimil(0)
verapimil(+)
d-sotalol(0)
d-sotalol(+)
l-sotalol(0)
l-sotalol(+)
dofetilide(0)
dofetilide(+)
haloperidol(0)
haloperidol(+)
amiodarone(0)
amiodarone(+)
ibogaine(0)
ibogaine(+)
ibogalog #119(0)
ibogalog #119(+)
tabernanthalog(0)
tabernanthalog(+)
E-4031(0)
E-4031(+)
clozapine(0)
NS1643(0)
moxifloxacin(0)
moxifloxacin(±)
quinidine(0)
quinidine(+)
perhexiline(0)
perhexiline(+)
nifekalant(0)
nifekalant(+)
ΔG_{bind} (R.E.U.)
0
−20
OPEN
INACT.
CLOSED

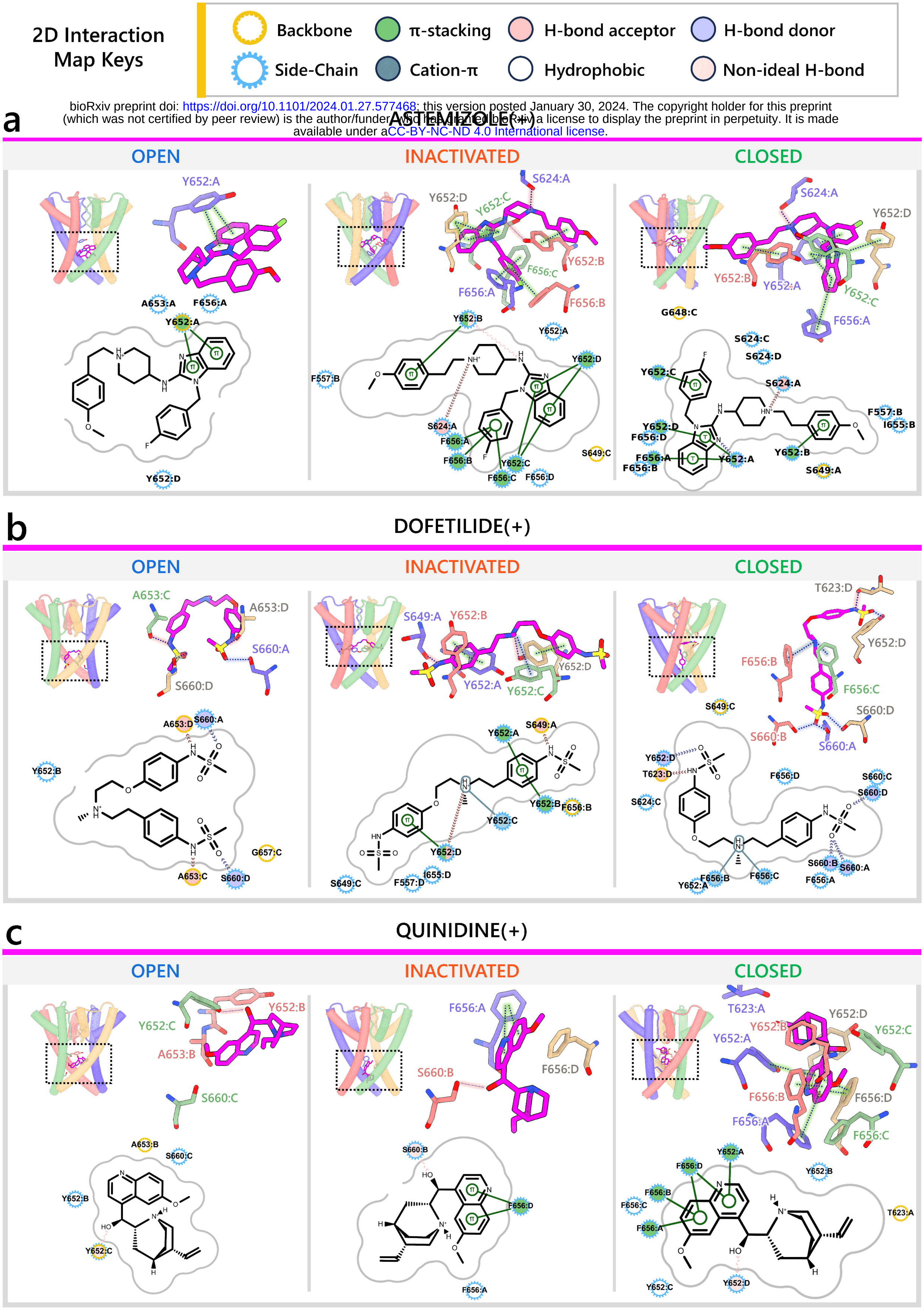
2D Interaction Map Keys
Backbone
π-stacking
H-bond acceptor
H-bond donor
Side-Chain
Cation-π
Hydrophobic
Non-ideal H-bond
a
ASTEMIZOLE(+)
OPEN
INACTIVATED
CLOSED
Y652:A
A653:A
F656:A
Y652:D
Y652:C
S624:A
F656:C
Y652:B
F656:B
F557:B
S649:C
F656:D
G648:C
S624:C
S624:D
I655:B
S649:A
b
DOFETILIDE(+)
OPEN
INACTIVATED
CLOSED
A653:C
A653:D
S660:A
S660:D
Y652:B
G657:C
S649:A
Y652:A
Y652:C
Y652:D
F656:B
I655:D
F557:D
S649:C
T623:D
F656:C
S660:B
S660:C
F656:D
S624:C
F656:A
c
QUINIDINE(+)
OPEN
INACTIVATED
CLOSED
Y652:B
Y652:C
A653:B
S660:C
F656:A
S660:B
F656:D
T623:A
Y652:D
Y652:A
F656:B
F656:C

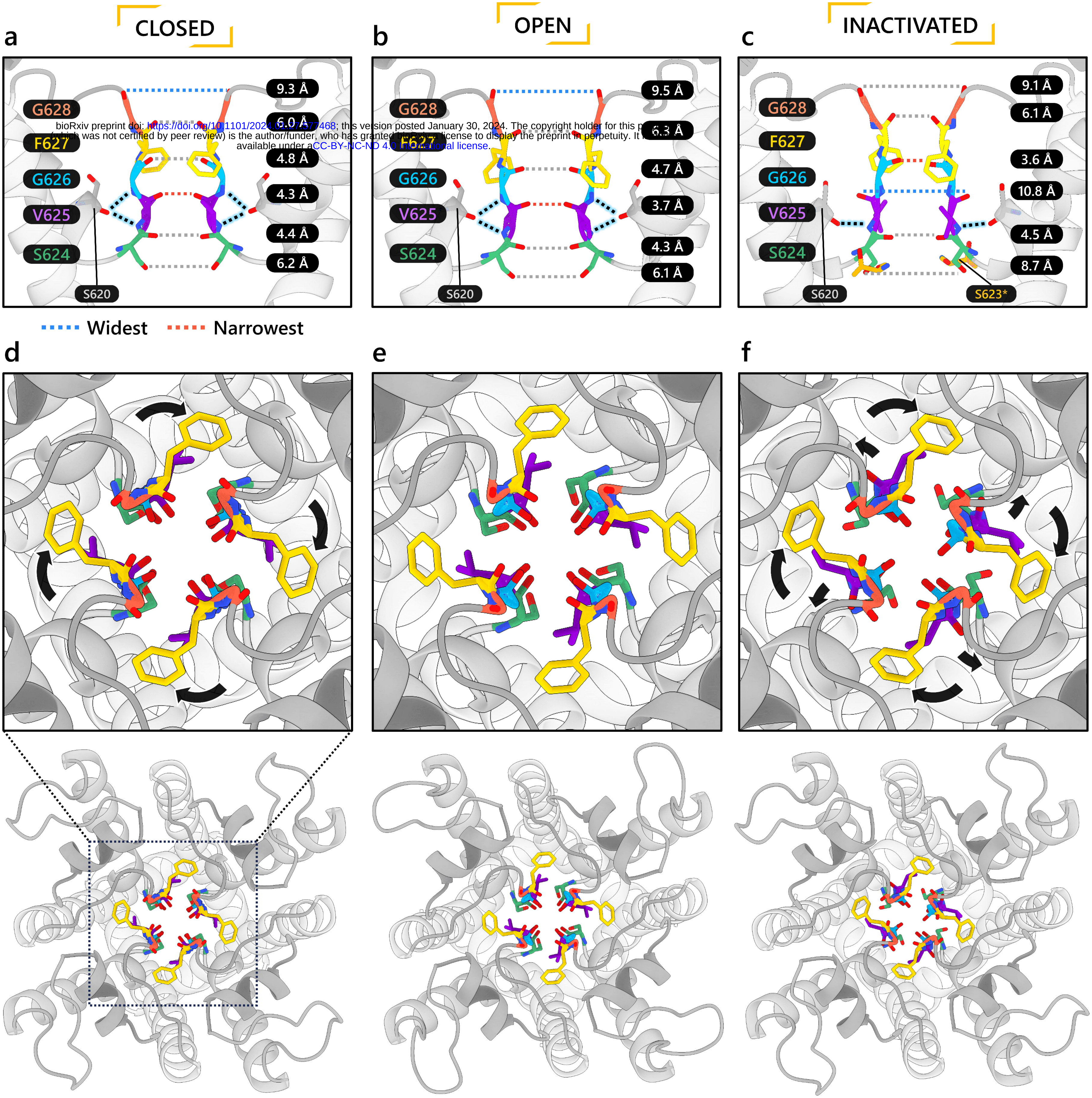
a
CLOSED
G628
F627
G626
V625
S624
S620
9.3 Å
6.0 Å
4.8 Å
4.3 Å
4.4 Å
6.2 Å
b
OPEN
G628
F627
G626
V625
S624
S620
9.5 Å
6.3 Å
4.7 Å
3.7 Å
4.3 Å
6.1 Å
c
INACTIVATED
G628
F627
G626
V625
S624
S620
S623*
9.1 Å
6.1 Å
3.6 Å
10.8 Å
4.5 Å
8.7 Å
Widest
Narrowest
d
e
f

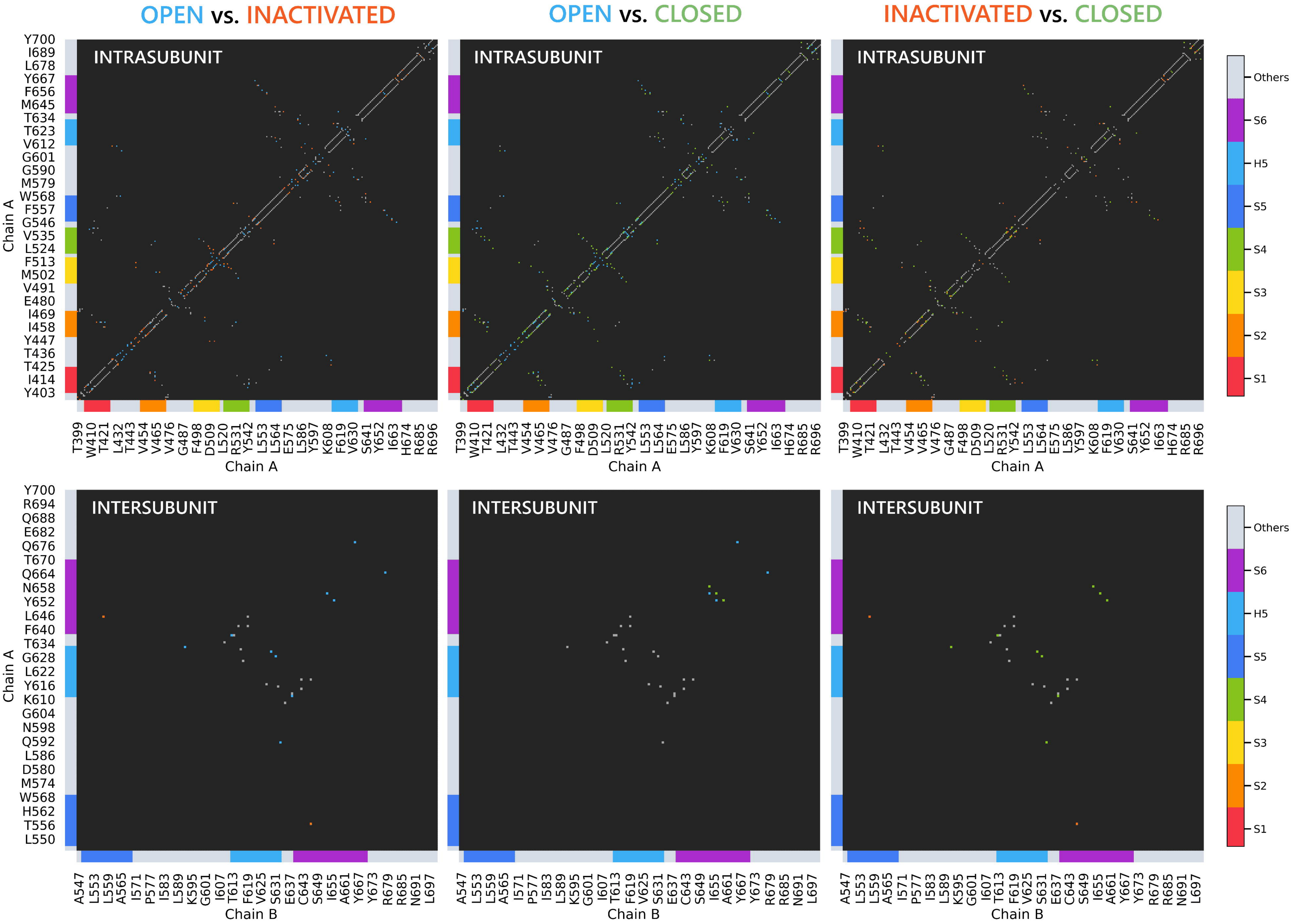
OPEN vs. INACTIVATED
OPEN vs. CLOSED
INACTIVATED vs. CLOSED
INTRASUBUNIT
INTERSUBUNIT
Chain A
Chain B
Y700
I689
L678
Y667
F656
M645
T634
T623
V612
G601
G590
M579
W568
F557
G546
V535
L524
F513
M502
V491
E480
I469
I458
Y447
T436
T425
I414
Y403
T399
W410
T421
L432
T443
V454
V465
V476
G487
F498
D509
L520
R531
Y542
L553
L564
E575
L586
Y597
K608
F619
V630
S641
Y652
I663
H674
R685
R696
R694
Q688
E682
Q676
T670
Q664
N658
Y652
L646
F640
T634
G628
L622
Y616
K610
G604
N598
Q592
L586
D580
M574
W568
H562
T556
L550
A547
L553
L559
A565
I571
P577
I583
L589
K595
G601
I607
T613
F619
V625
S631
E637
C643
S649
I655
A661
Y667
Y673
R679
R685
N691
L697
Others
S6
H5
S5
S4
S3
S2
S1

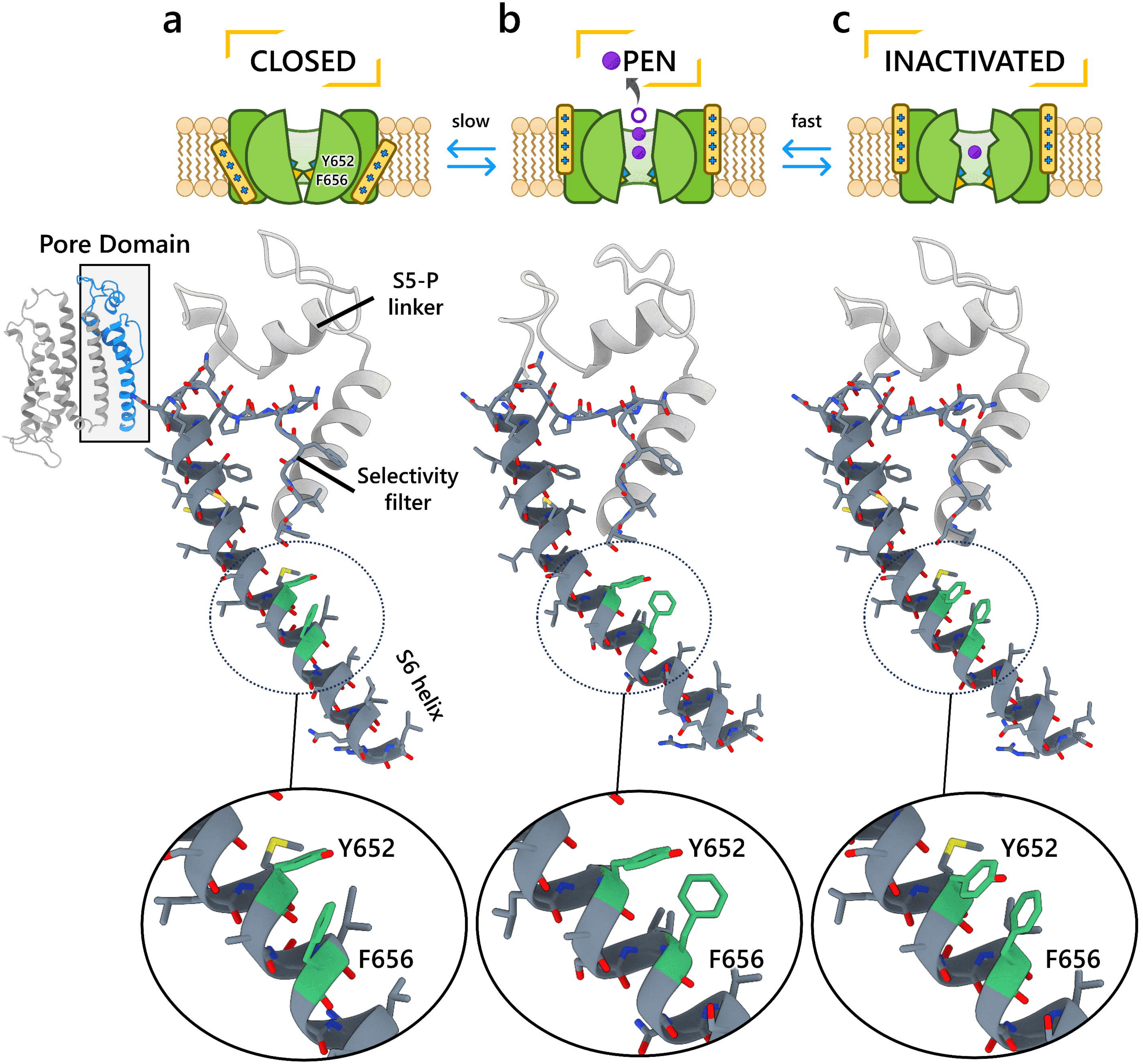
a
CLOSED
b
OPEN
c
INACTIVATED
slow
fast
Y652
F656
Pore Domain
S5-P linker
Selectivity filter
S6 helix
Y652
F656
Y652
F656
Y652
F656

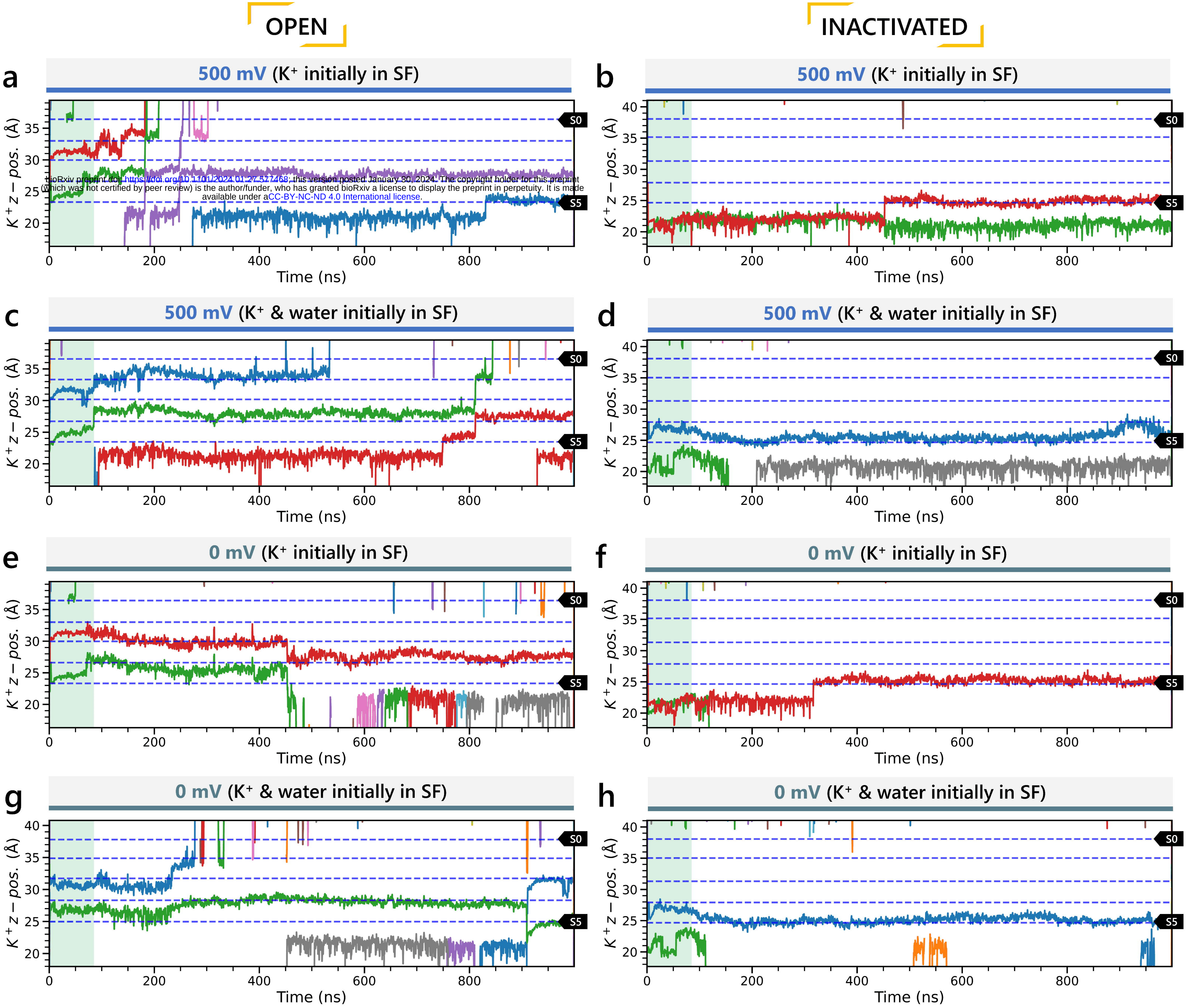
OPEN
INACTIVATED
a
500 mV (K⁺ initially in SF)
b
500 mV (K⁺ initially in SF)
c
500 mV (K⁺ & water initially in SF)
d
500 mV (K⁺ & water initially in SF)
e
0 mV (K⁺ initially in SF)
f
0 mV (K⁺ initially in SF)
g
0 mV (K⁺ & water initially in SF)
h
0 mV (K⁺ & water initially in SF)
$K^+ z-pos.$ (Å)
Time (ns)
S0
S5
0
200
400
600
800
20
25
30
35
40

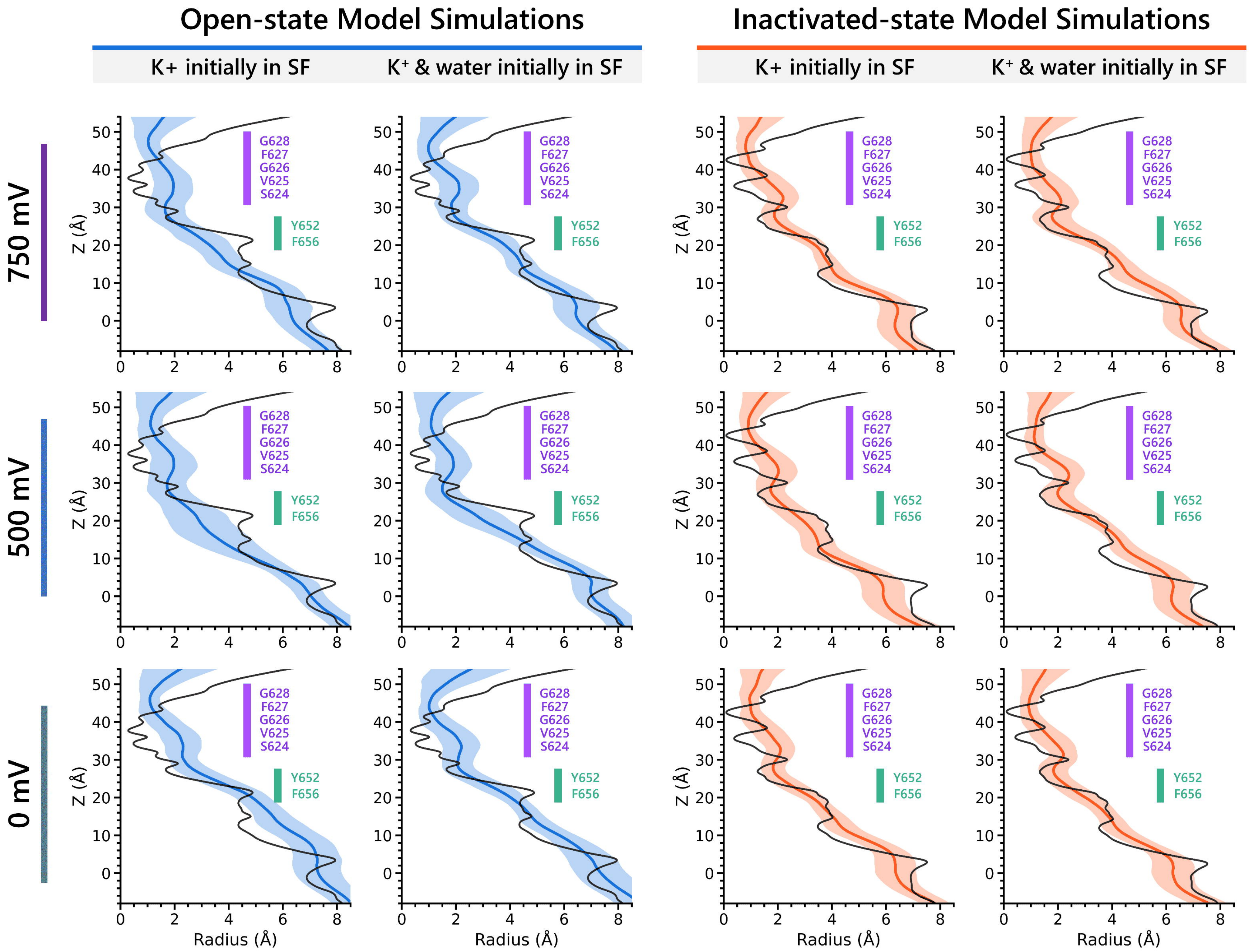
Open-state Model Simulations
Inactivated-state Model Simulations
K+ initially in SF
K⁺ & water initially in SF
K+ initially in SF
K⁺ & water initially in SF
750 mV
500 mV
0 mV
Z (Å)
50
40
30
20
10
0
Radius (Å)
0
2
4
6
8
G628
F627
G626
V625
S624
Y652
F656